Global Environmental Science
www.sciltp.com/journals/ges

Review

Continuously Selective Oxidation of Hydrogen Sulfide over Carbon-Nitrogen Catalysts for Sustainable Environment—A Review

Hanfeng Ye [1,†], Fei Zhao [2,†], Shihuan Lyu [3], Zhiqi Wen [4,5], Dapeng Wu [6,*] and Can Yang [4,5,*]

1 College of Chemistry and Chemical Engineering, Taiyuan University of Technology, Taiyuan 030024, China
2 School of Chemical Engineering and Technology, Taiyuan University of Science and Technology, Taiyuan 030024, China
3 School of Chemical and Environmental Engineering, Hunan Institute of Technology, Hengyang 421000, China
4 State Key Laboratory of Chemistry for NBC Hazards Protection, College of Chemistry, Fuzhou University, Fuzhou 350116, China
5 State Key Laboratory of Photocatalysis on Energy and Environment, College of Chemistry, Fuzhou University, Fuzhou 350116, China
6 School of Environment, Key Laboratory for Yellow River and Huai River Water Environment and Pollution Control, Ministry of Education, Henan Normal University, Xinxiang 453007, China
* Correspondence: dapengwu@htu.edu.cn (D.W.); canyang@fzu.edu.cn (C.Y.)
† These authors contributed equally to this work.

How To Cite: Ye, H.; Zhao, F.; Lyu, S.; et al. Continuously Selective Oxidation of Hydrogen Sulfide over Carbon-Nitrogen Catalysts for Sustainable Environment—A Review. *Glob. Environ. Sci.* **2026**, *2*(1), 1–22. https://doi.org/10.53941/ges.2026.100001

Publication History

Received: 5 October 2025
Revised: 17 November 2025
Accepted: 24 November 2025
Published: 8 December 2025

Keywords

hydrogen sulfide;
continuously selective oxidation;
carbon-nitrogen catalysts;
sustainable environment

Highlights

- Modified carbon-nitrogen catalysts boost reactant adsorption and product desorption
- Kinetics insights, in situ experiments and density functional theory establish the structure-activity relationship and elucidate catalytic mechanism
- Future research focus on the scalability and stability of carbon-nitrogen catalysts

Abstract: Hydrogen sulfide (H_2S), a highly toxic and corrosive gas emitted from natural, industrial and agricultural processes, poses severe risks to human health, infrastructure, and environment safety. Although the traditional Claus process has been widely used for H_2S removal, thermodynamic constraints lead to the residue of 3–5% H_2S in the tail gas, necessitating advanced technologies for further transformation and purification. Continuously selective oxidation of H_2S (H_2S-CSO) has emerged as a promising technology that can achieve near-complete sulfur recovery and ensure compliance with emission regulations. Carbon-nitrogen catalysts show significant potential to replace metal-based catalysts in the H_2S-CSO process due to their tunable electronic structures, cost-effectiveness, and resistance to sulfur poisoning. This review comprehensively summarizes the major milestones in the development of carbon-nitrogen catalysts for H_2S-CSO process. We focus on key advances, including construction of active sites (e.g., pyridinic N and metal single atoms), regulation of surface electronic structure (e.g., via elemental doping and defect engineering), the use of supports, optimization of pore structure to facilitate both reactants (H_2S and O_2) adsorption and sulfur desorption processes. These modifications are critically discussed in relation to catalytic performance and stability, so as to unveil the underlying structure-activity relationships. Despite these advances, review articles dedicated to carbon-nitrogen catalysts for H_2S-CSO remain scarce, and this work aims to fill that gap. Current challenges such as sulfur poisoning, SO_2 over-oxidation, and catalyst scalability are addressed, along with future directions for the rational design of robust carbon-nitrogen catalysts aimed at sustainable H_2S treatment and sulfur resource recovery.

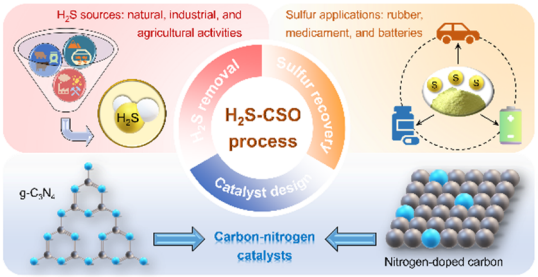

1. Introduction

H_2S, a highly toxic and flammable acidic gas, originates from diverse natural and anthropogenic sources, such as volcanic emissions, biological decomposition, and various industrial and agricultural activities (Figure 1) [1–3]. With escalating global fossil fuel consumption, industrial H_2S emissions have evolved into a pressing environmental and economic issue. Notably, H_2S is detectable by its characteristic rotten-egg odor at concentrations as low as 10 ppb. Prolonged exposure to low concentrations can induce adverse health effects, while levels exceeding 500 ppm may cause rapid loss of consciousness, fatal respiratory paralysis, and death [4–6]. Beyond its direct health hazards, H_2S also triggers severe corrosion in pipelines, valves, and industrial equipment, and leads to the rapid deactivation of metal-based catalysts, incurring substantial economic losses. Moreover, the atmospheric oxidation of H_2S produces sulfur dioxide (SO_2), a primary precursor to acid rain, thereby exacerbating environmental damage [7–9]. Consequently, the development of efficient and economical technologies for H_2S removal is imperative.

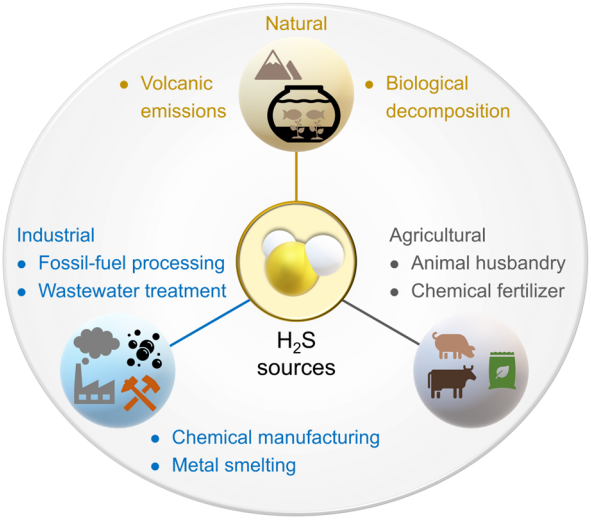

Figure 1. Schematic diagram of H_2S sources.

For nearly a century, wet absorption processes employing alkaline solutions (e.g., ammonia or amine-based solvents) have been widely utilized for H_2S capture. However, the high operational costs of these methods stem not only from the non-regenerative nature of many absorbents but also from the reversible absorption in regenerative processes that allow H_2S re-release [10–12]. The Claus process, patented in 1883, emerged as a dominant technology for H_2S elimination and sulfur recovery. This process is suitable for high-concentration H_2S scenarios to achieve sulfur recovery at industrial scale, which involves the partial oxidation of H_2S to SO_2 (Equation (1)), followed by its reaction with remaining H_2S over catalysts to form elemental sulfur (Equation (2)). Despite its widespread adoption, the Claus process is constrained by thermodynamic limitations, typically achieving only 60–70% conversion per catalytic stage. This necessitates multiple reactors in series to attain an overall sulfur recovery efficiency of ~98%, yet the resultant tail gas still contains 3–5% H_2S, requiring further treatment [13–15].

$$H_2S + 3/2O_2 \rightarrow SO_2 + H_2O \qquad \Delta H = -519\ kJ/mol \quad (1)$$

$$2H_2S + SO_2 \rightarrow 3/nS_n + 2H_2O \qquad \Delta H = -147\ kJ/mol \quad (2)$$

$$H_2S + 1/2O_2 \rightarrow 1/nS_n + H_2O \qquad \Delta H = -222\ kJ/mol \quad (3)$$

To address residual H_2S, enhanced catalytic technologies such as the Mobil Direct Oxidation Process and Super Claus have been developed and commercialized [16,17]. These systems rely on the direct selective oxidation of H_2S to sulfur (H_2S-CSO process, Equation (3)), which offers several distinct advantages: absence of thermodynamic equilibrium limitations, reduced SO_2 emissions, high sulfur selectivity, lower operating temperatures, tolerance to moisture, ease of integration into existing infrastructure, applicability to various feed compositions, and no hydrogen consumption [18–20]. As illustrated in Figure 2, the H_2S-CSO process enables near-complete sulfur recovery and ensures compliance with stringent emission regulations.

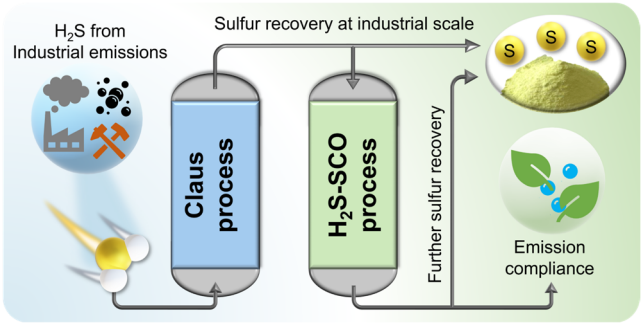

Figure 2. Schematic diagram of H_2S removal from industrial sources.

In recent years, significant research efforts have been devoted to developing more efficient heterogeneous catalysts for H_2S selective oxidation, such as metal-based catalysts (e.g., oxides, carbides, sulfides), carbon-based catalysts, zeolites, metal organic frameworks, covalent triazine frameworks, and layered double hydroxides [17,20–26]. Owing to their superior intrinsic activity, extensive research has primarily focused on metal-based catalysts for H_2S-CSO process. However, their performance is frequently hampered by deactivation mechanisms including metal sulfidation, pore blockage by sulfur deposits, and active-site coverage by sulfate species [27–30]. These persistent challenges have motivated the exploration of nonmetal alternatives. Carbon-based materials, particularly activated carbon (AC), have garnered significant interest due to their low cost, high

specific surface area (SSA), tunable porosity, and demonstrated efficacy in low-temperature H_2S removal [31–33]. Nevertheless, the conventional low-temperature H_2S removal process is inherently discontinuous, as accumulated sulfur must be periodically desorbed, requiring reactor shutdown and catalyst regeneration [34–36]. Transitioning to a continuous operation mode demands temperatures above the sulfur dew point to facilitate sulfur evaporation. Under such conditions, most AC catalysts exhibit limited activity due to a scarcity of active sites for H_2S activation [37–39]. Furthermore, their predominantly microporous structure often impedes sulfur diffusion, thereby promoting over-oxidation to SO_2 [40–42]. Recently, carbon-nitrogen catalysts, especially nitrogen-doped carbon (NDC), have shown considerable promise. The incorporation of nitrogen functional groups (e.g., pyridinic N) serves as the Lewis basic site that enhances H_2S dissociation and moderate local pH. This synergistic effect promotes sulfur migration from micropores to larger pores, thereby improving desorption kinetics and suppressing SO_2 formation [43,44].

Given their promising activity, the application of carbon-nitrogen catalysts in the H_2S-CSO process has become increasingly noteworthy. This review provides a comprehensive overview of the development, catalytic performance, and mechanistic insights of carbon-nitrogen catalysts for the H_2S-CSO process. We systematically summarize the synthetic strategies, modified strategies, catalytic performance and underlying mechanism of these catalysts, with a particular emphasis on the role of active sites and pore structure in promoting the adsorption of reactants (H_2S and O_2) and the desorption of sulfur products. Furthermore, we critically examine the relationships between catalyst properties (e.g., element doping, surface chemistry, pore structure, and electronic configuration) and catalytic performance under various conditions, such as high O_2 concentrations or elevated reaction temperatures. This review also addresses persistent challenges in the fields, such as achieving long-term stability under industrial conditions, suppressing over-oxidation, and scaling up catalyst production. By evaluating recent experimental and theoretical advances, this work aims to guide the rational design of high-performance carbon-nitrogen catalysts and to accelerate their practical implementation for efficient H_2S removal and sustainable sulfur recovery, ultimately contributing to cleaner industrial processes and environment protection.

2. Advancements in Carbon-Nitrogen Catalysts for Continuous H_2S-CSO Process

2.1. Synthetic Strategies of Carbon-Nitrogen Catalysts

Since the 1980s, NDC materials have garnered significant interest due to their capacity to modulate the atomic and electronic structures of the carbon matrix, thereby enhancing electrical conductivity and tailoring chemical reactivity [45,46]. The nitrogen functionalities in these materials are broadly classified into two categories: (i) surface-dangling groups, such as amines (–NH_2, –NH–, –N=), nitro (–NO_2), nitroso (–NO), and cyano (–C≡N); and (ii) framework-incorporated species, including pyridinic N, pyrrolic N, graphitic N, and pyridinic N-oxide (Figure 3a) [34]. Surface-dangling groups are typically introduced via low-temperature pyrolysis (400–500 °C) of AC or carbon nanotubes (CNTs) under NH_3 atmosphere or in the presence of urea [47]. These nitrogen-modified carbons exhibit a higher H_2S adsorption heat (50 kJ/mol) compared to their unmodified counterparts (10–40 kJ/mol), which facilitates H_2S capture [48]. However, their practical application is hampered by limited content (usually below 10%) and stability during long-term H_2S-CSO process, typically resulting in irreversible functional loss [49,50].

To achieve more stable nitrogen incorporation within the carbon framework, strategies such as high-temperature pyrolysis (around 900 °C) under NH_3 or pyridine for AC and CNTs, as well as chemical vapor deposition (CVD), have been employed [51–53]. Owing to the higher electronegativity of nitrogen (χ = 3.04) compared to carbon (χ = 2.55), framework-incorporated pyridinic N acts as a Lewis basic site with considerable thermal stability [34]. This functionality modulates the local pH and enhances surface polarity, thereby promoting H_2S adsorption [54,55]. A direct correlation between pyridinic N content and H_2S uptake was evidenced by Sun et al. [43]. Furthermore, the electron-donating character of pyridinic N significantly strengthens O_2 activation, contributing to markedly improved H_2S-CSO performance [56]. For instance, Ghasemy et al. demonstrated that N-doped CNTs, even with a limited pyridinic N content, achieved complete H_2S conversion (~100%) at 230 °C, vastly outperforming pristine CNTs (~28%) [57].

Conventional doping strategies, however, often face limitations in either nitrogen content or scalability and cost [53]. In response, research has shifted toward intrinsically nitrogen-rich carbon-based catalysts. Graphite carbon nitride (g-C_3N_4), a metal-free polymer with a high theoretical nitrogen content (57.1 at%), has emerged as a promising candidate for the H_2S-CSO process (Figure 3b) [58,59]. In a seminal 2018 study, Shen et al. reported the first application of g-C_3N_4 catalysts in this process, where an optimal sample (CNM-600) achieved a sulfur yield of 93% at 180 °C, far exceeding that of a commercial Fe_2O_3 catalyst (~17%) [60]. The potential for scalable synthesis and practical application of g-C_3N_4 is underpinned by two key advantages: (i) the diversity of low-cost precursors (e.g., urea, thiourea, dicyandiamide, melamine, cyanuric acid and trithiocyanuric acid) and (ii) a relatively simple preparation process (often involving direct pyrolysis in air) [61]. Inspired by g-C_3N_4, other N-rich polymers have been explored. Lei et al. reported the first use of carbon-doped boron nitride for the H_2S-CSO process, demonstrating high sulfur yield and corrosion

resistance [62]. A covalent triazine framework derived from the self-polymerization of 1,4-dicyanobenzene was shown to outperform bulk g-C_3N_4 across the entire reaction temperature range [25]. Mi et al. developed pyridinic N-functionalized hierarchical porous polymers via the copolymerization of vinylbenzyl chloride and 4-vinylpyridine, realizing 100% H_2S conversion at 180 °C [63].

Beyond g-C_3N_4, the direct pyrolysis of nitrogen-rich precursors—such as biomass, conductive polymers, and metal organic frameworks—represents a dominant pathway for NDC synthesis. The resulting catalysts typically feature high SSA and well-developed porosity, which facilitate H_2S adsorption, sulfur desorption, and the exposure of active nitrogen sites [64–66]. In contrast to the limited porosity of g-C_3N_4, these NDC catalysts generally possess higher SSA and more developed pore structure. This hierarchical porosity not only ensures full exposure of doped nitrogen species, but also promotes mass transport, accounting for the enhanced catalytic performance (Figure 3c) [67]. Furthermore, the tunable electronic structure of NDC catalysts allows for co-doping with other heteroatoms (e.g., B, P, S) to fine-tune performance under specific conditions [68–70]. Their compatibility with various supports (e.g., CNTs and silicon carbide) further underscores their versatility and potential for scalable industrial implementation [53,71].

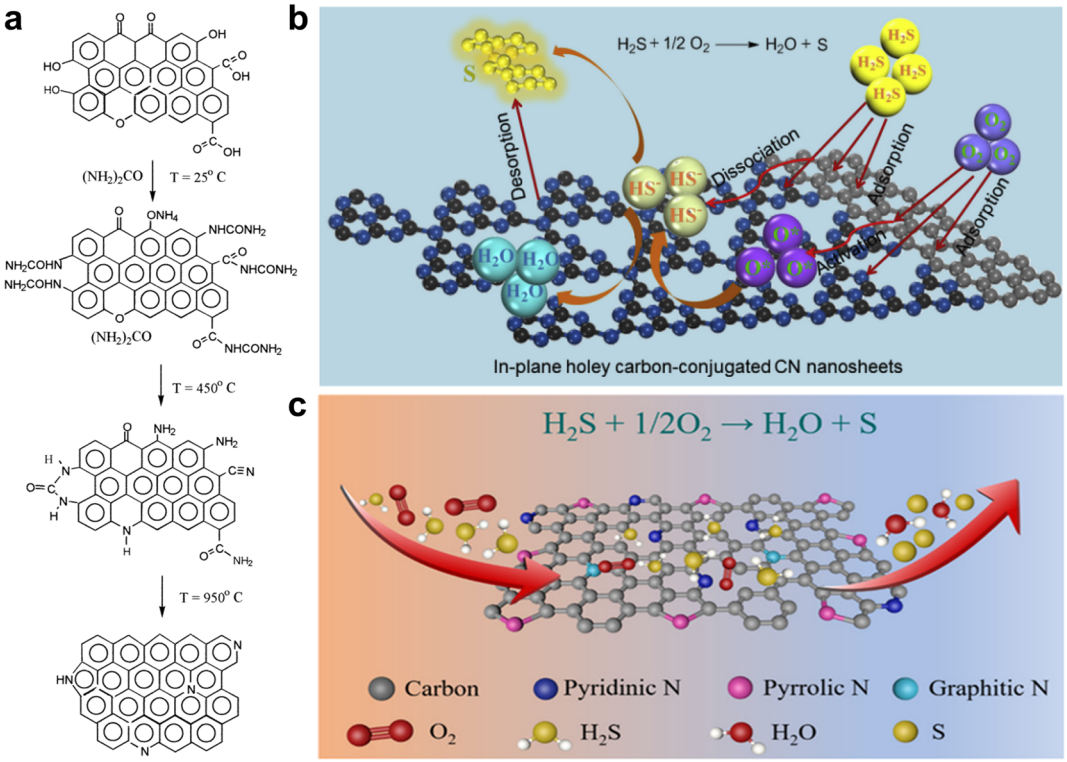

Figure 3. (**a**) Schematic representation of different types of nitrogen species in carbon-nitrogen catalysts. Reproduced with permission. Copyright 2000, American Chemical Society [34]. (**b**) H_2S-CSO process over g-C_3N_4 catalysts. Reproduced with permission. Copyright 2019, Elsevier [59]. (**c**) H_2S-CSO process over NDC catalysts. Reproduced with permission. Copyright 2021, American Chemical Society [67].

For both g-C_3N_4 and NDC catalysts, their inherent nitrogen sites are propitious for loading and anchoring metal species, enabling the construction of well-defined active sites. A prevalent and straightforward strategy is the one-step pyrolysis of a mixture containing a carbon-nitrogen precursor and a metal salt [17,72]. During the thermal treatment under an inert atmosphere, the simultaneous carbonization, nitrogen doping, and in situ reduction of the metal ions occur, leading to the formation of metal species uniformly dispersed within the N-rich matrix, as demonstrated in the synthesis of metal single-atom (e.g., Fe and Co) catalysts on g-C_3N_4 and Co nanoparticles encapsulated by N-doped carbon layers [73–76]. Subsequent density functional theory (DFT) studies on such models, like Co–N_x and Fe–N_x (x = 3 or 4) doped graphene, confirm these M–N_x configurations as the active centers for H_2S and O_2 activation [77–79]. An alternative approach involves a two-step process, where N-doped carbon nanotube (N-CNT) is first synthesized and subsequently functionalized to introduce surface groups that facilitate the uniform deposition of molybdenum (Mo) precursors via incipient wetness impregnation, followed by a calcination step to form well-dispersed MoO_x on N-CNT [80]. Furthermore, a coordination-assisted pyrolysis strategy has been effectively utilized, as exemplified by the synthesis of Mn–N_4 single-atom catalysts. Mn ions are first coordinated with a nitrogen-rich resin, and the subsequent pyrolysis in the presence of fumed silica, followed by acid and alkali etching, yields a porous NDC

matrix with atomically dispersed Mn–N_4 sites, demonstrating the versatility of precursor design in creating defined coordination environments [81]. These synthetic pathways collectively leverage the inherent affinity of nitrogen sites in the carbon framework for metal species, enabling the precise construction of highly active and stable catalysts for H_2S-CSO process.

2.2. Modified Strategies of Carbon-Nitrogen Catalysts

2.2.1. g-C_3N_4 Catalysts

Despite the abundance of amino functional groups in graphitic carbon nitride (g-C_3N_4), which facilitates H_2S adsorption, its extended π-conjugated electronic structure—arising from the sp^2 hybridization of carbon and nitrogen—results in a lack of active sites for O_2 adsorption and activation. Furthermore, the inherent tendency of π−conjugated layers to stack via van der Waals interactions and hydrogen bonding leads to the formation of bulk morphologies with low SSA [61]. These structural limitations impede the desorption of elemental sulfur, causing surface deposition and rapid catalyst deactivation. To overcome these challenges, researchers have pursued systematic optimization of g-C_3N_4 through synthesis process control, micro-nanostructure regulation, surface modification, and electronic structure modulation.

To disrupt the stacked bulk architecture, Lei et al. exfoliated bulk g-C_3N_4 via secondary thermal treatment, obtaining ultrathin nanosheets with a thickness of only 1.02 nm as evidenced by transmission electron microscopy (TEM) and atomic force microscopy (AFM) images (Figure 4a–e) [82]. Such thickness is much smaller than bulk g-C_3N_4 (~2.5 nm, Figure 4f,g) [83]. The diminished intensity of XRD diffraction peaks and the blue shift of the absorption edge in DRS spectra further confirmed successful exfoliation. The resulting material exhibited an increased SSA from 41 to 156 m^2/g, and its sulfur yield at 180 °C improved by 3.9-fold relative to bulk g-C_3N_4. However, the durability of the exfoliated catalyst remained limited, sustaining activity for only 4 h, which was attributed to insufficient pore volume and persistent sulfur accumulation. To address pore structure limitations, Kamali et al. employed SBA-15 as a hard template to synthesize g-C_3N_4 nanorods with a high SSA of 525 m^2/g (Figure 4h,i). These nanorods functioned as nanoreactors that enhanced mass transfer, achieving 99.8% H_2S conversion, while shortened diffusion pathways promoted sulfur desorption, yielding 88.8% sulfur selectivity. The catalyst lifetime was extended to 20 h. A key challenge of this approach, however, lies in the template removal step, which requires hazardous hydrofluoric acid, thereby complicating the synthesis and impeding scalable production [84].

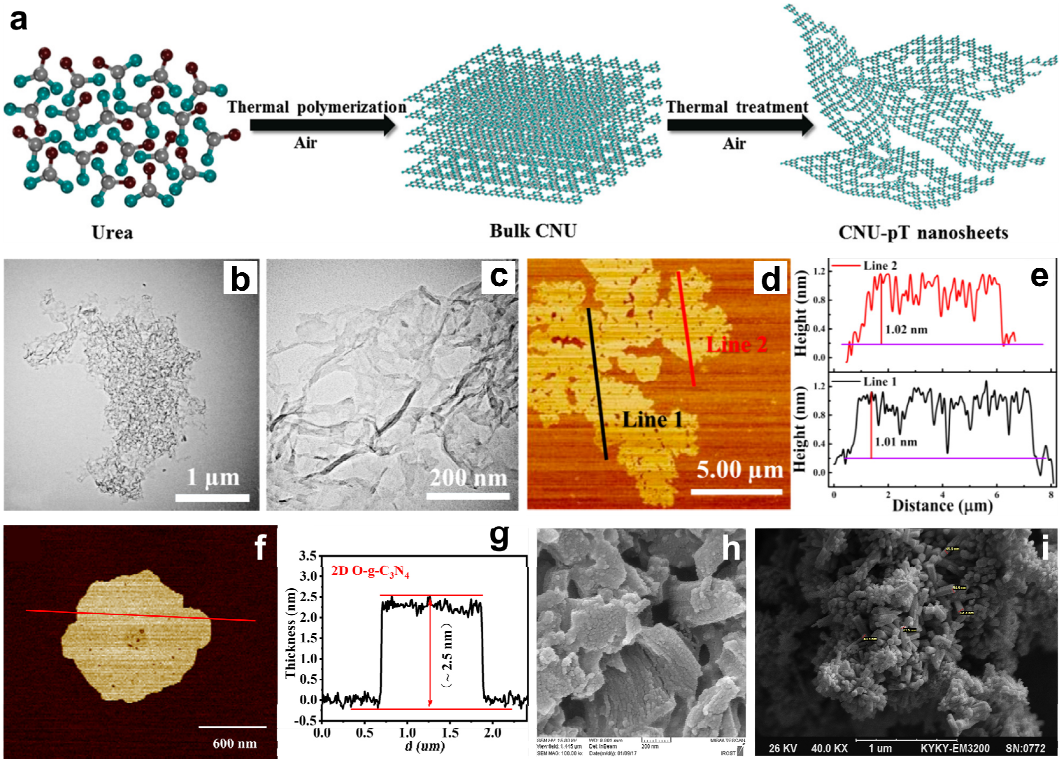

Figure 4. (**a**) Illustration of the processes for the generation of exfoliated g-C_3N_4 catalysts. (**b**,**c**) TEM images, (**d**) AFM image, and (**e**) height scanning of CNU-p600. Reproduced with permission. Copyright 2019, American Chemical Society [82]. (**f**) AFM image of 2D O-g-C_3N_4 and (**g**) the corresponding thickness analysis. Reproduced with permission. Copyright 2022, IOP Publishing [83]. SEM images of (**h**) bulk and (**i**) nanorod g-C_3N_4 catalysts. Reproduced with permission. Copyright 2019, Elsevier [84].

Beyond morphological control, electronic structure modulation represents a powerful strategy to strengthen reactant adsorption and enhance catalytic performance. Lei et al. pyrolyzed a mixture of urea and cetyltrimethylammonium bromide (CTAB) to obtain carbon-conjugated g-C_3N_4 porous nanosheets (Figure 5a). CTAB served a dual role: as a carbon source that extended the π−electron system and as a soft template whose thermal decomposition generated in situ porosity. This synergistic modification significantly enhanced the adsorption of both H_2S and O_2, leading to a sulfur yield of 97.9% at 180 °C and a lifetime of 24 h [59]. In an alternative approach, Lyu et al. directly doped carbon atoms into the g-C_3N_4 framework. This not only expanded the π−conjugated system, but also introduced unpaired electrons and induced structural distortion in the stacked layers, creating active sites for H_2S and O_2 adsorption and activation. The optimized catalyst ($CNG_{0.2}$) achieved 99% H_2S conversion and 95% sulfur selectivity at 200 °C, with a durability exceeding 70 h. Notably, $CNG_{0.2}$ was synthesized on a large scale using low-cost melamine and glucose while retaining comparable catalytic performance (Figure 5b), demonstrating promise for practical application [85].

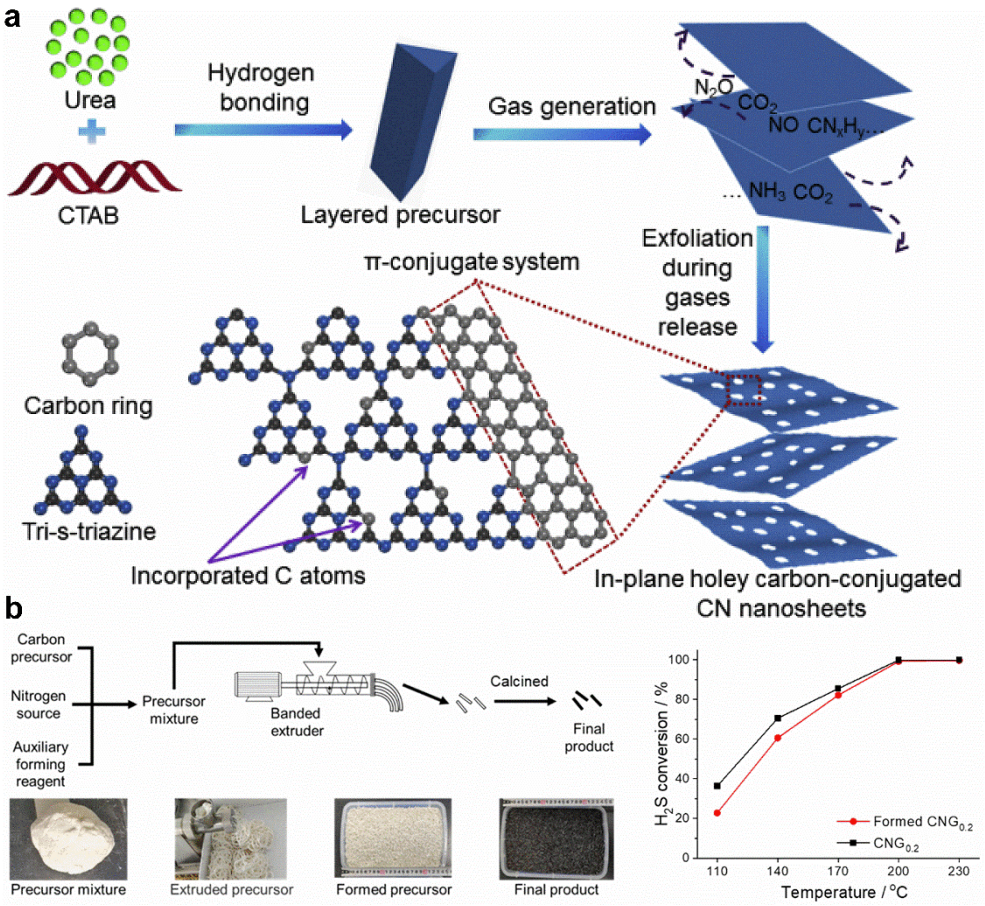

Figure 5. (**a**) Schematic illustration for the generation of in-plane holey carbon-conjugated CN nanosheets. Reproduced with permission. Copyright 2019, Elsevier [59]. (**b**) The fabrication process of formed $CNG_{0.2}$ and corresponding H_2S conversion compared to $CNG_{0.2}$. Reproduced with permission. Copyright 2022, Elsevier [85].

Building on the success of carbon modification, Shen et al. grafted bromophenyl functional groups onto the g-C_3N_4 framework. This modification delocalized the π-conjugation and enhanced the basicity of nitrogen active sites, thereby promoting H_2S dissociation and reducing affinity for adsorbed sulfur. These electronic and structural optimizations collectively enabled simultaneous high H_2S conversion (100%) and sulfur selectivity (100%), along with an extended lifetime of 200 h [86]. Besides metal-free modifications, Lei et al. modified g-C_3N_4 with Mo_2C. Combined experimental and theoretical studies revealed that Mo_2C induced charge redistribution in the g-C_3N_4 framework, strengthening H_2S adsorption on adjacent N sites and achieving a sulfur yield of 99% at 190 °C [21]. These studies underscore the versatility of electronic modulation strategies for both metal-free and metal-modified g-C_3N_4 catalysts.

Compared to metal-free modification, the Mo_2C-modified g-C_3N_4 exhibited a shorter lifetime of only 30 h, possibly due to sulfur poisoning of the metal sites. It is well-known that nitrogen-rich motifs in g-C_3N_4 can effectively disperse and stabilize metal species, forming single-atom catalysts (SACs). Such architectures offer multiple advantages: (i) enhanced metal stability and

sulfur tolerance, (ii) reduced metal usage and cost, (iii) effective modulation of the π–conjugated electronic structure to promote reactant adsorption and activation, and (iv) well-defined active sites conducive to establishing structure-activity relationships [72,87]. In this regard, Lei et al. developed a g-C_3N_4-supported Fe–N_4 SAC with a flaky morphology, in which Fe single atoms were clearly observed at both narrow and wide scales and had little influence on the inherent structure of g-C_3N_4 (Figure 6) [73]. Compared to its nanoparticle counterpart (a sulfur yield of ~40% and a lifetime of 20 h), the Fe SAC exhibited markedly superior performance (~99% sulfur yield at 180 °C) and durability (270 h). By varying precursor compositions, the valence state of Fe could be precisely tuned: Fe SACs derived from dicyandiamide and $FeCl_3$ featured exclusively Fe^{3+} (Figure 6a), whereas those from trithiocyanuric acid and iron (II) phthalocyanine contained a mixture of Fe^0 and Fe^{2+} (Figure 7a). The dual-valence Fe SAC achieved higher sulfur yield (~99%) than the single-valence analogue (~82%), which was attributed to accelerated redox cycling between adjacent valence states [73,74]. Further enhancement was achieved by substituting Fe with Co single atoms (Figure 7b), which attained 100% H_2S conversion and a lifetime of 460 h, alongside excellent thermal stability and tolerance to typical industrial gas components such as H_2O, SO_2, CO_2, and H_2 (Figure 7c) [75].

Besides transition metals, Lyu et al. applied a molten salt method to synthesize a crystalline poly(triazine imide) intercalated with lithium ions (PTI-Li^+), representing the first use of crystalline carbon nitride in the H_2S-CSO process (Figure 8a). In contrast to the melon structure of conventional g-C_3N_4, PTI-Li^+ exhibits a well-defined crystalline framework, enabling clearer correlation between structure and activity. The interaction between atomically dispersed Li sites and the triazine framework enhances electron delocalization and modulates the electronic band structure, thereby promoting the adsorption and activation of both O_2 and H_2S (Figure 8b–f). As a result, PTI-Li^+ achieved 98% H_2S conversion and 98% sulfur selectivity at 200 °C, with a durability of approximately 100 h [88]. All above works confirm superior stability of metal single atoms in the H_2S-CSO process.

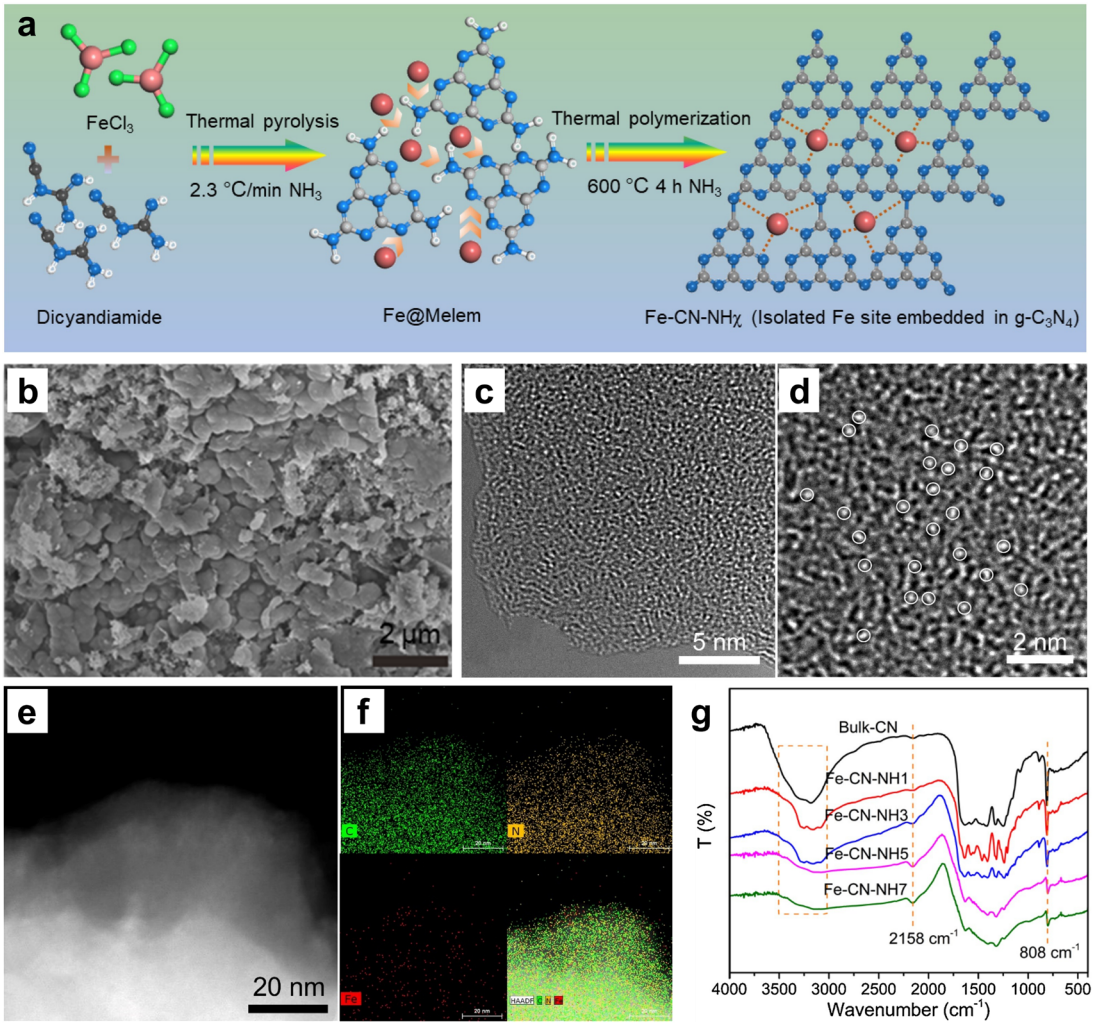

Figure 6. (**a**) Pyrolytic synthesis of Fe-CN-NH_χ catalysts. (**b**) SEM image, (**c**,**d**) HAADF-STEM images, and (**e**,**f**) the corresponding element mappings of Fe-CN-NH5 catalyst. (**g**) FT-IR profiles of Fe-CN-NH_χ catalyst. Reproduced with permission. Copyright 2020, Elsevier [73].

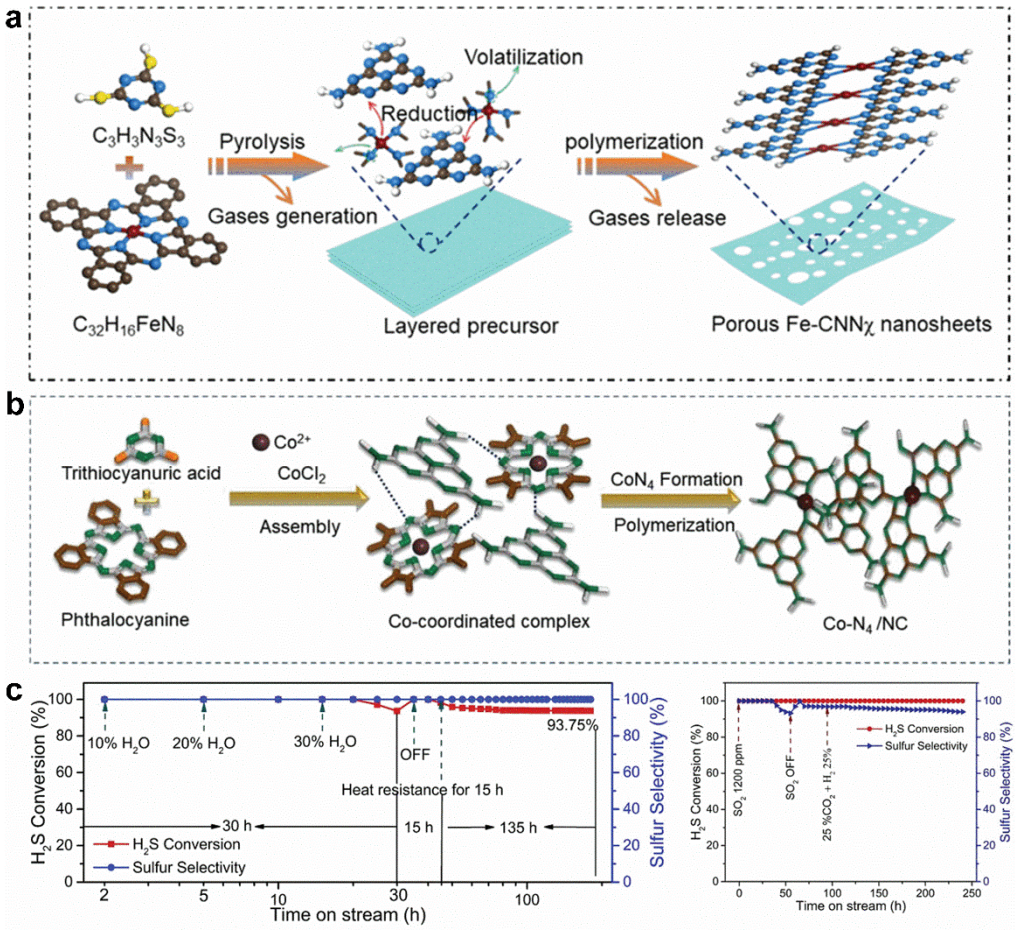

Figure 7. (**a**) Fabrication scheme of Fe-CNN$_\chi$ catalysts. Reproduced with permission. Copyright 2020, Wiley-VCH [74]. (**b**) Illustration of the process for the preparation of Co–N_4/NC catalysts and (**c**) corresponding catalytic performance on impurities (H_2O, SO_2, CO_2 and H_2) and heat resistance. Reproduced with permission. Copyright 2021, Wiley-VCH [75].

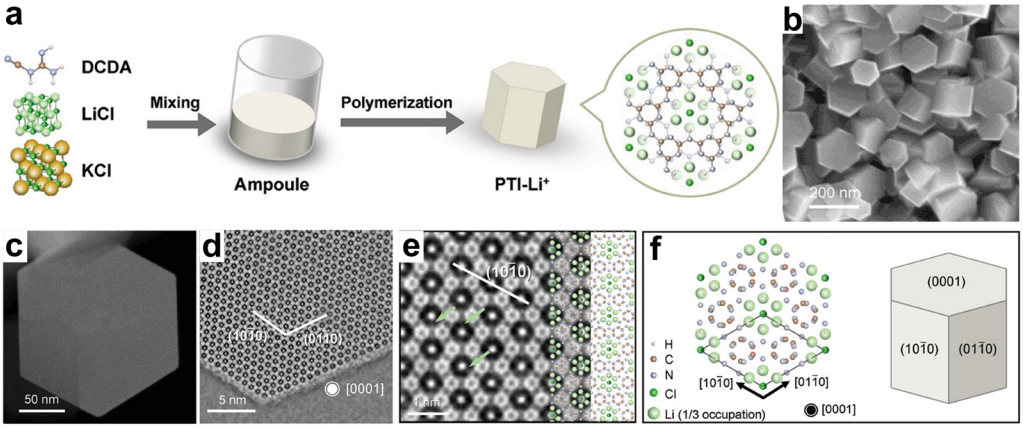

Figure 8. (**a**) Preparation and structure of PTI-Li$^+$ and corresponding (**b**) SEM image, (**c**) HAADF-STEM image, (**d**) AC-iDPC image along the [0001] direction, as well as (**e**) expanded view of (**d**), (**f**) the crystal structure and the schematic diagram of a PTI-Li$^+$ crystal. Reproduced with permission. Copyright 2024, Wiley-VCH [88].

2.2.2. NDC Catalysts

Similar to g-C_3N_4, pristine carbon materials possess a π-conjugated electronic structure arising from sp^2-hybridized carbon, which inherently lacks active sites for the adsorption and activation of both H_2S and O_2. Initial efforts to enhance their catalytic performance in the H_2S-CSO process focused on direct acid treatment to introduce oxygen-containing functional groups. While this approach led to significant initial improvements, the poor durability of these oxygen groups—stemming from their reaction with H_2S to form H_2O—limited their practical utility [38,89,90]. In contrast, nitrogen doping, which leverages the comparable atomic sizes of N and C, provides a more robust means of modulating the surface electronic

structure of carbon matrices, thereby effectively promoting the co-adsorption and activation of H_2S and O_2 [54,56].

Early applications of NDC catalysts in H_2S-CSO primarily involved nitrogen-doped CNTs (N-CNTs) synthesized via CVD. A marked enhancement in H_2S conversion was observed, increasing from 2% for undoped CNTs to 99.8% for N-CNTs [53]. To address reactor pressure drop issues, Ba et al. scaled up N-CNTs into macroscale spherical particles using an alginate gel method. The gel framework contributed to an elevated SSA and meso-macroporous structure. However, the spherical N-CNTs exhibited diminished H_2S conversion and sulfur selectivity compared to the pristine powder. This decline was attributed to CNT entanglement within the spheres, which reduced the accessible SSA, limited active site exposure, and impeded sulfur desorption. The prolonged residence time of sulfur within the porous network subsequently promoted its over-oxidation to SO_2 [91].

To mitigate these issues, N-CNTs were supported on macroscopic silicon carbide (N-CNTs/SiC) with various geometries (e.g., particles, extrudates, foams, rings). N-CNTs/SiC demonstrated superior H_2S conversion (~95%) compared to its unsupported counterpart (~35%) at 190 °C (Figure 9a–f). This enhancement was ascribed to the improved spatial distribution of N-CNTs within the catalytic bed, ensuring more efficient contact between reactants and active sites. SiC foam supports, in particular, induce turbulence that enhances gas mixing. A critical finding was that higher catalyst loadings do not invariably yield better performance, as excessive loading can impede reactant access to active sites (Figure 9g,h), underscoring the advantage of supports in optimizing catalyst utilization [92–94]. Further improvement was achieved by Wang et al., who replaced conventional Joule heating with non-contact induction heating, thereby boosting H_2S conversion [95]. Although SiC supports enhanced H_2S conversion, sulfur selectivity often declined, likely due to extended sulfur residence time facilitating over-oxidation. Introducing toluene into the feed gas effectively mitigated this issue by increasing the solubility of elemental sulfur, thereby accelerating its removal from mesopores and suppressing SO_2 formation [96].

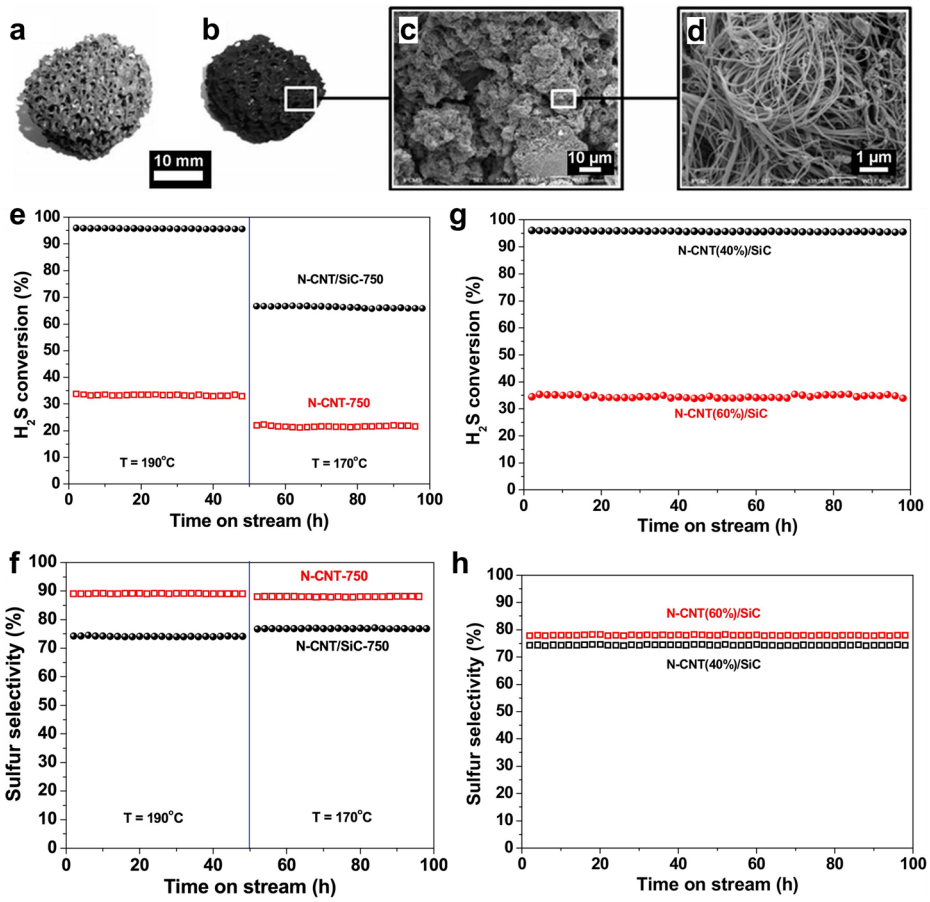

Figure 9. Photographs of (**a**) SiC foam and (**b**) N-CNT/SiC foam composite. (**c**,**d**) SEM images of N-CNT/SiC composite. Reproduced with permission. Copyright 2012, Wiley-VCH [53]. (**e**) H_2S conversion and (**f**) sulfur selectivity on N-CNT/SiC-750 and N-CNT-750 catalysts. (**g**) H_2S conversion and (**h**) sulfur selectivity on N-CNT/SiC with different N-CNT loading. Reproduced with permission. Copyright 2014, Elsevier [94].

Despite these advances, the aforementioned strategy faces two primary challenges: (i) the high cost of SiC supports and (ii) the typically low nitrogen content of CVD-synthesized N-CNTs, which necessitates reaction temperatures above 200 °C for satisfactory H_2S conversion, increasing energy consumption. To address these

limitations, Li et al. employed low-cost CNTs as tunable supports. Pyrolysis of nitrogen-rich precursors mixed with CNTs yielded NDC catalysts with a relatively high nitrogen content (8.4 at%), achieving 99.4% H_2S conversion at 190 °C [71]. Inspired by this, Wang et al. treated waste AC with melamine and formed monolithic N-AC catalysts using lotus root starch gel. These macroscopic catalysts achieved approximately 90% H_2S conversion and sulfur selectivity, outperforming their powdered equivalents [97]. Besides CNTs and AC, Liu et al. employed electrospinning of polyacrylonitrile and polyvinylpyrrolidone followed by pyrolysis to produce macroscopic NDC catalysts with high nitrogen content (10.8 at%) and excellent durability exceeding 200 h [98].

A dominant methodology for synthesizing NDC catalysts involves the direct pyrolysis of carbon- and nitrogen-containing compounds with templating agents (e.g., alkalis, salts) to maximize SSA, thereby exposing more nitrogen active sites and creating defects that enhance reactant adsorption and activation. Li et al. used KOH as an activator to prepare an NDC catalyst with an ultrahigh SSA of 3530 m^2/g, rich in defects and nitrogen (Figure 10a). Experimental results indicated that defect density increased with melamine content, while nitrogen content decreased at higher pyrolysis temperatures (Figure 10b,c). Catalytic performance in the H_2S-CSO process exhibited positive correlations with both defect density and pyridinic N content. Consequently, the EM-3.5-800 catalyst, pyrolyzed at a relatively low temperature (800 °C), exhibited high defect density and pyridinic N content, achieving optimal performance (97.7% H_2S conversion and 90.2% sulfur selectivity) [44]. Liu et al. further demonstrated the synergistic role of defects and pyridinic N, wherein pyridinic N enhanced H_2S adsorption while defects promoted O_2 activation into superoxide radicals [99]. Apart from KOH, Liu et al. utilized NaCl as a template to fabricate porous NDC catalysts. The addition of NaCl dramatically increased the SSA from 41 m^2/g (NC-0-800) to 502 m^2/g (NC-10-800), with defect density increasing concomitantly with NaCl content. The NC-10-800 catalyst maintained high H_2S conversion (~96%) and sulfur selectivity (91%) over a 100-h stability test, indicating excellent stability of the defective structure. Differential charge density analysis revealed greater charge accumulation for both H_2S and O_2 adsorbed on defective NDC surfaces compared to defect-free models (Figure 10d,e). These defects significantly enhanced the Lewis basicity of pyridinic N, and promoted the adsorption and activation of both H_2S and O_2, thereby improving overall H_2S-CSO performance [100,101].

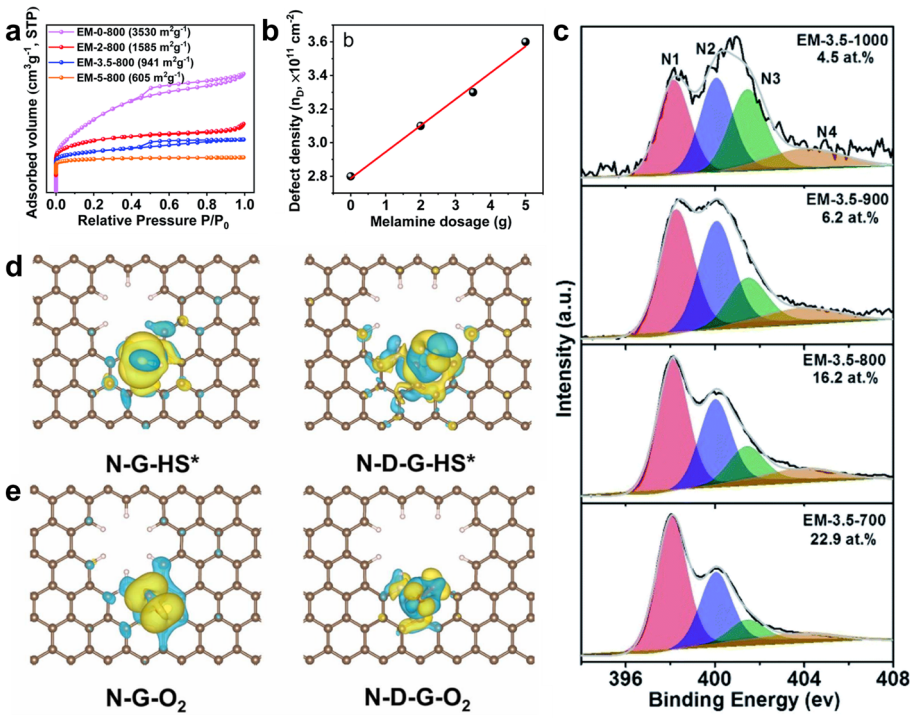

Figure 10. (**a**) Nitrogen adsorption-desorption isotherms of the N-doped carbon nanoflakes synthesized with different melamine concentrations. (**b**) defect density of samples with different melamine mass. (**c**) High-resolution N 1s spectra and the contents of different nitrogen species of N-doped carbon nanoflakes prepared at different temperatures. Reproduced with permission. Copyright 2020, Royal Society of Chemistry [44]. 3D differential charge densities of (**d**) HS* and (**e**) O_2 on N-G and N-D-G. The yellow and blue isosurfaces correspond to the increase in the number of electrons and the depletion zone, respectively. Reproduced with permission. Copyright 2026, Elsevier [101].

Considering that template removal complicates the synthesis process and hinders scalability, Yang et al. directly pyrolyzed thermally stable polyaniline (PANI) in air without templates, obtaining an NDC catalyst (NrC-

450) with high nitrogen content (17.2 wt.%) and developed porosity (474 m^2/g). The air atmosphere facilitated the conversion of PANI to NDC at relatively low temperatures (>350 °C), markedly reducing energy consumption (Figure 11a). Benefiting from high pyridinic N content and developed pore structure, the optimal NrC-450 catalyst achieved 99.6% H_2S conversion and 93.4% sulfur yield, demonstrating excellent stability over 72-h [64]. Inspired by this work, various polymers, including copolymer, polypyrene, and polyimide, have been employed as precursors to prepare NDC catalysts with superior H_2S-CSO performance, highlighting the promise of polymeric precursors [67,102,103]. Beyond synthetic polymers, biomass represents another important source for NDC catalysts, with materials such as waste air-laid paper, discarded cigarette butts, and biochar already applied in H_2S-CSO process (Figure 11b) [65,104,105].

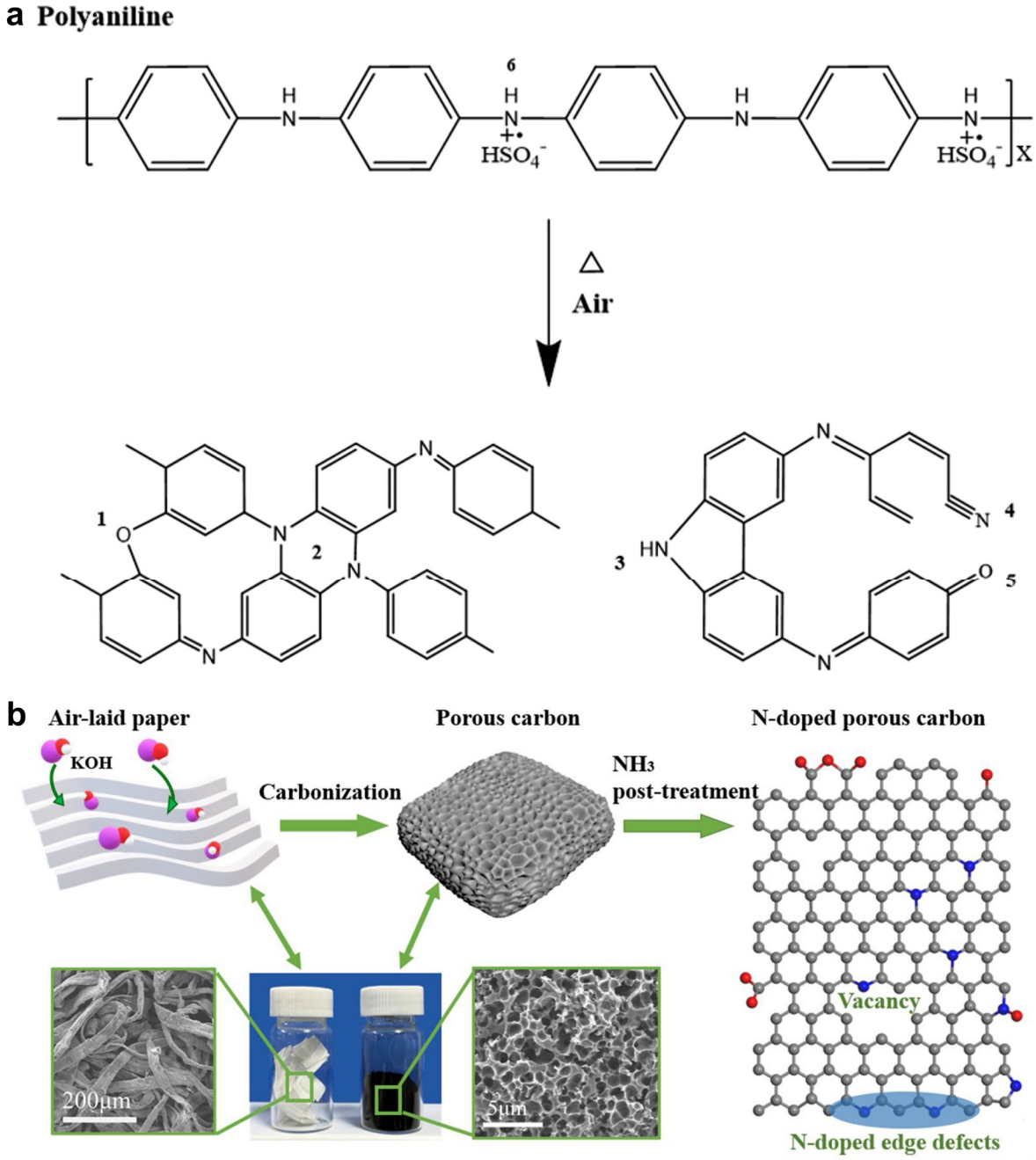

Figure 11. (**a**) Possible chemical changes accompanying the thermal treatment of polyaniline leading to the formation of (1) ether, (2) phenazine rings, (3) pyrrolic N, (4) nitrile groups, (5) ketone, and (6) quaternary N. Reproduced with permission. Copyright 2020, American Chemical Society [64]. (**b**) Schematic fabrication process for N-doped porous carbon from waste air-laid paper. Reproduced with permission. Copyright 2021, Elsevier [65].

A catalytic reaction encompasses reactant adsorption/activation, conversion, and product desorption. In the H_2S-CSO process, the catalytic performance depends not only on the efficiency of H_2S

adsorption and conversion, but also critically on the rate of sulfur desorption. Due to capillary effects, both reactant H_2S molecules (3.72 Å) and product sulfur molecules (8.06 Å) tend to adsorb and deposit in catalyst micropores (Figure 12a). If sulfur is not promptly desorbed, it inevitably undergoes over-oxidation to SO_2 and block H_2S access, reducing both H_2S conversion and sulfur selectivity. To address this, Li et al. prepared an NDC catalyst with an interconnected micro-mesoporous network. The abundant mesopores facilitated rapid H_2S diffusion to active sites located in micropores, while greatly enhancing the diffusion and desorption of sulfur transferred from micropores via nitrogen species. This hierarchical structure enabled the catalyst to achieve 100% H_2S conversion and approximately 90% sulfur selectivity at an extremely high weight hourly space velocity (WHSV) of 60,000 mL g^{-1} h^{-1} for over 160 h [106,107]. Building on the concept of mesoporosity, Zhang et al. synthesized NDC catalysts with tunable sizes (0.12–1.06 μm) by controlling the size of zeolitic imidazolate framework (ZIF) precursors. The resulting catalysts possessed similar SSA, pore size, and nitrogen content, enabling the establishment of a size-activity relationship. Results indicated that smaller particle sizes promoted higher H_2S conversion but lower sulfur selectivity, likely due to enhanced active site exposure and improved reactant diffusion, coupled with severe particle stacking that prolonged sulfur-O_2 contact time and promoted over-oxidation [66]. Consequently, selecting larger ZIF-8 particles (0.89 μm) and adding NaCl as a protective agent during pyrolysis effectively mitigated nitrogen loss at high temperatures and further enhanced the interconnected micro-mesoporous structure (Figure 12b). This optimized catalyst achieved high H_2S conversion (96.5%) and sulfur selectivity (93.5%) at a WHSV (60,000 mL g^{-1} h^{-1}) [108]. The obtained product sulfur is the important raw materials for various value-added applications such as sulfuric acid, fertilizers, polymers [109,110].

While nitrogen species promote O_2 activation, this can lead to the over-oxidation of H_2S or sulfur to SO_2 under conditions of high O_2 concentration or temperature. However, the O_2/H_2S ratio in practical applications usually exceeds 0.5. To suppress over-oxidation, Liu et al. co-doped N and S atoms into the carbon matrix. The incorporated S atoms effectively reduced the Lewis basicity of pyridinic N, moderately weakening the adsorption of both H_2S and O_2. This adjustment enabled 94.3% H_2S conversion and 84.5% sulfur selectivity at an O_2/H_2S ratio of 2.5. though selectivity dropped sharply to 70.0% at a ratio of 7.5 [69]. To further improve performance, phosphate groups were modified onto an NDC catalyst. Temperature-programmed desorption (TPD) and O_2 reduction experiments revealed that phosphate groups mitigated O_2 adsorption capacity. Furthermore, the interaction between pyridinic N and phosphate groups, combined with a steric hindrance effect, inhibited sulfur accumulation around active sites, thus preventing over-oxidation. This design yielded a superior sulfur selectivity of 93% at an O_2/H_2S ratio of 12.5, although H_2S conversion was limited to ~85%, likely because excess O_2 covered the sites for H_2S adsorption [68]. To achieve both high H_2S conversion and sulfur selectivity under high O_2 conditions, Ye et al. developed a series of metal single atoms supported on NDC (M-NDC) to tailor the surface electronic structure and systematically screened the effect of metal identity on the adsorption energy of H_2S and O_2. Mn-NDC was identified as the optimal catalyst, maintaining over 90% H_2S conversion and 90% sulfur selectivity even at an O_2/H_2S ratio of 10 (Figure 13a). Importantly, this ratio can be attained by direct dilution with air, significantly simplifying the process and enhancing practical applicability. *Quasi*-in situ XPS analysis revealed that the rapid redox cycling between Mn^{2+} and Mn^{3+} species during the conversion of H_2S and O_2 underpinned high catalytic performance across a wide range of O_2/H_2S ratios (Figure 13b) [81]

For high-temperature operations, Ye et al. prepared N-P co-doped carbon (P-NDC) catalysts. Combined experimental and theoretical calculations revealed that compared to C atoms (χ = 2.55), N (χ = 3.04) and P (χ = 2.19) atoms function as Lewis base (LB) and Lewis acid (LA) sites, respectively. Their spatial separation within the carbon matrix facilitated the formation of Lewis pairs (LPs). These LPs significantly enhanced the chemisorption of both H_2S and SO_2 molecules, effectively promoting the Claus reaction (Figure 13c). Consequently, the P-NDC catalyst achieved excellent sulfur yields of 97.4% at 240 °C and 95.7% at 260 °C, demonstrating potential as an alternative to traditional metal-based catalysts and filling the application gap for carbon-based catalysts in the H_2S-CSO process within the 200–300 °C range [70].

To provide a clearer overview and facilitate a direct comparison of the various g-C_3N_4 and NDC catalysts discussed in this section, Table 1 summarizes their key physicochemical properties (e.g., specific surface area and nitrogen content) alongside their catalytic performance in the H_2S-CSO process. This systematization helps to elucidate the structure-property-performance relationships that govern the design of efficient H_2S-CSO catalysts.

 https://doi.org/10.53941/ges.2026.100001

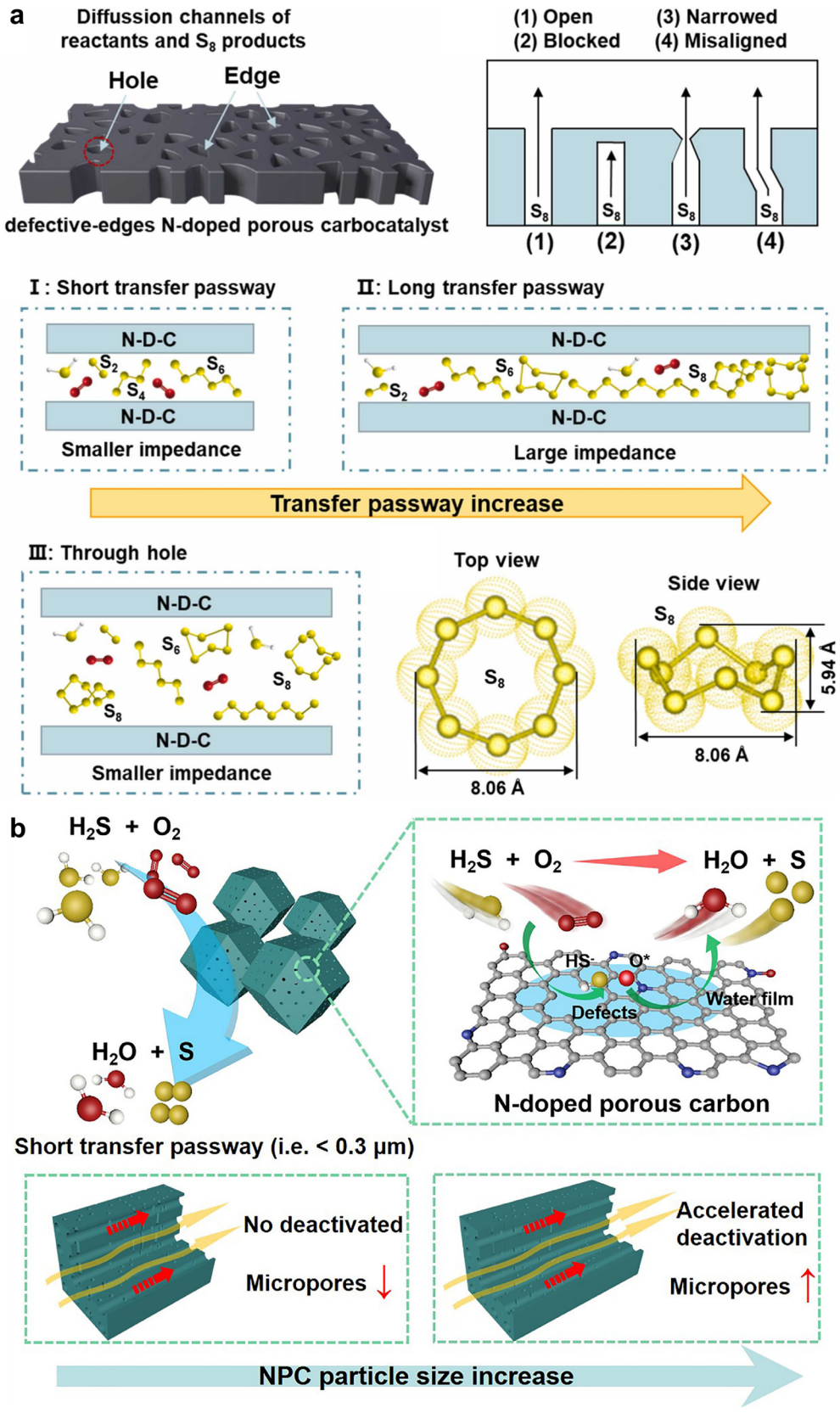

Figure 12. (**a**) Illustration of sulfur cluster diffusion in the pore structures of the fabricated defective-edges N-doped porous carbocatalyst during H_2S-CSO process: the transfer processes of the reactants (H_2S and O_2) and products (polysulfides, S_2, S_4, S_6 and S_8 molecules) in different types of porous structure: I, a short transfer pathway in microporous carbon; II, a long transfer pathway in microporous carbon; III, mesoporous carbon. Reproduced with permission. Copyright 2024, Elsevier [106]. (**b**) Schematic illustration of the reaction pathway and critical parameters of size-controllable NPC carbocatalysts for H_2S selective oxidation. Reproduced with permission. Copyright 2021, Elsevier [66].

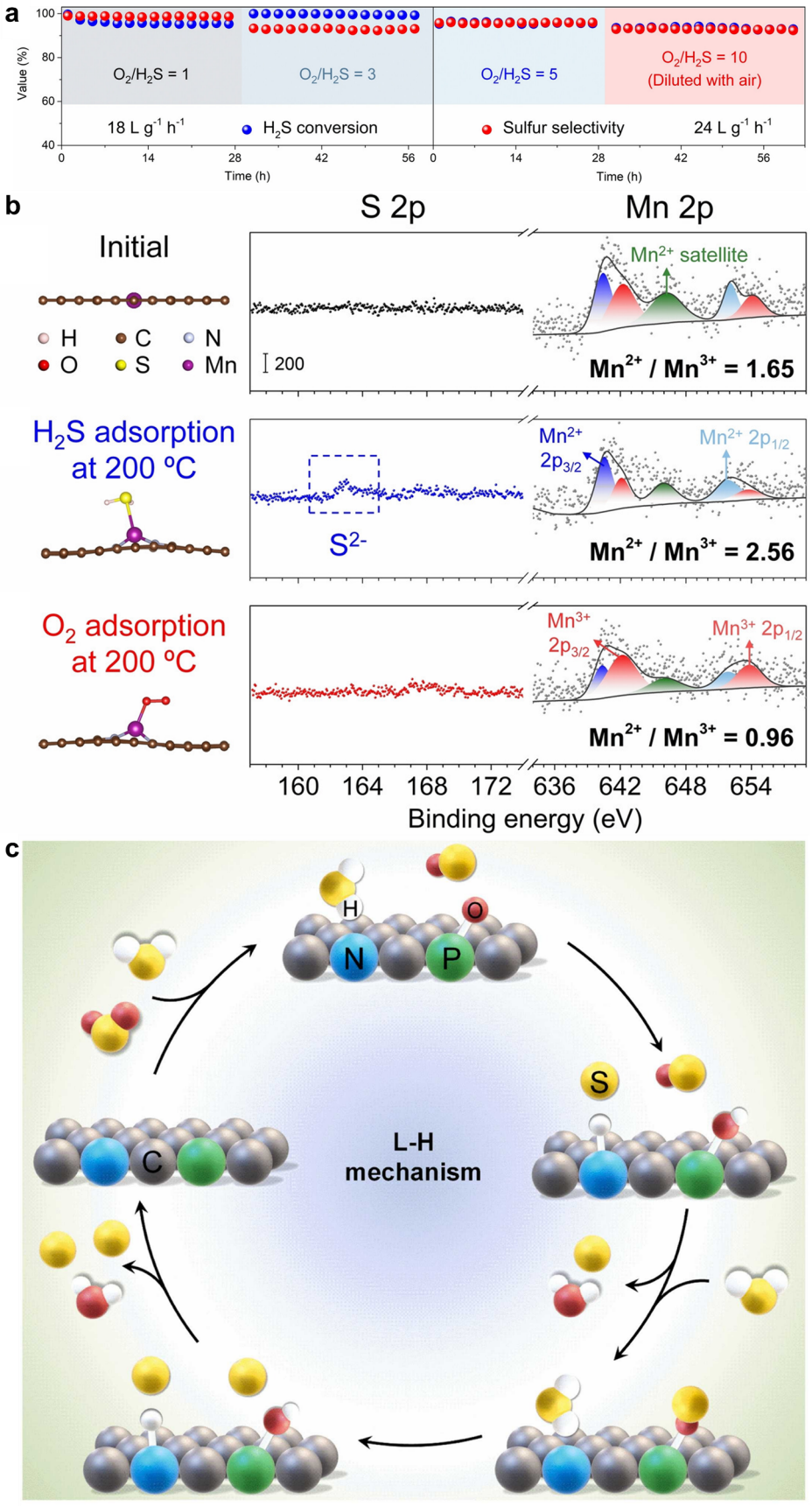

Figure 13. (**a**) The durability test of Mn-NDC in H_2S-CSO process in different O_2/H_2S and WHSV at 200 °C. (**b**) High-resolution XPS S 2p and Mn 2p spectra of Mn-NDC under different conditions: initial state, after H_2S adsorption at 200 °C and after O_2 adsorption at 200 °C. Reproduced with permission. Copyright 2025, Wiley-VCH [81]. (**c**) Potential mechanism of Claus reaction on P-NDC. Reproduced with permission. Copyright 2025, Elsevier [70].

 https://doi.org/10.53941/ges.2026.100001

Table 1. Comparison of physicochemical properties and catalytic performance of reported g-C3N4 and NDC catalysts in the H_2S-CSO process.

Class	Samples	S_{BET} (m^2/g)	N Content	WHSV/GHSV	T (°C)	H_2S Conv.	S Sel.	Lifetime (h)	Refs.
$g\text{-}C_3N_4$	CNM-600	114.1	51.7 at%	3 L g^{-1} h^{-1}	180	97%	96%	4	[60]
	CNU-p600	156.0	62.1 wt%	3 L g^{-1} h^{-1}	180	74.5%	100%	4	[82]
	MCNR	524.6	/	1200 h^{-1}	190	99.8%	88.8%	30	[84]
	PCNUC5	125.6	49.5 at%	3 L g^{-1} h^{-1}	210	100%	97.9%	24	[59]
	$CNG_{0.2}$	256	41 at%	12 L g^{-1} h^{-1}	200	99%	95%	70	[85]
	$CNU\text{-}Br_{75}$	99.8	/	3 L g^{-1} h^{-1}	180	100%	100%	200	[86]
	MC/CN	/	/	6 L g^{-1} h^{-1}	190	99%	100%	30	[21]
	Fe-CN-NH5	19.3	55.9 wt%	6 L g^{-1} h^{-1}	240	94.1%	100%	180	[73]
	Fe-CNN4	239.9	51.1 wt%	6 L g^{-1} h^{-1}	180	100%	99%	270	[74]
	4Co-N/NC	205.1	23.7	3 L g^{-1} h^{-1}	210	100%	97%	460	[75]
	PTI–Li^+	44	45.6 at%	6 L g^{-1} h^{-1}	200	98%	98%	100	[88]
NDC	$N\text{-}CNT_{2.6N}$	210	2.6 at%	0.32 h^{-1}	190	91%	75%	120	[53]
	N-CNT-750	205	2.4 at%	0.6 h^{-1}	190	35%	90%	50	[92,94]
	N-CNT/SiC-750	150	4.1 at%			95%	75%	50	
	N-CNTs	205	/	2400 h^{-1}	210	100%	83%	30	[91]
	N-CNT beads	237	/			98%	76%	30	
	NMC/SiC	54	/	2400 h^{-1}	190 (JH)	87%	82%	140	[95]
					190 (IH)	100%	77%	140	
	$N\text{-}C/CNT_{800}^{450}$	412	4.2 at%	0.6 h^{-1}	190	99.4%	79.2%	130	[71]
	N@AC-700	609	5.0 at%	20 L g^{-1} h^{-1}	190	93%	83%	50	[97]
	N@CF-800	20	10.8 at%	0.6 h^{-1}	230	57%	95%	200	[98]
	EM-3.5-800	941	16.2 at%	0.9 h^{-1}	190	97.7%	90.2%	80	[44]
	C-N-5	1768	3.1 at%	12 L g^{-1} h^{-1}	220	100%	95%	12	[99]
	NC-10-800	502	19 at%	60 L g^{-1} h^{-1}	190	96%	91%	100	[100]
	NDC-700	1442	19.5 at%	20 L g^{-1} h^{-1}	190	94.8	92.6 %	80	[101]
	NrC-450	474	17.2 wt%	6 L g^{-1} h^{-1}	180	99.6%	94%	72	[64]
	N-OMCS-700	1575	4.46 wt%	12 L g^{-1} h^{-1}	180	100%	92%	22	[102]
	PPy-KOH-700	3157	6.8 wt%	6 L g^{-1} h^{-1}	150	100%	97%	24	[67]
	HNMC-800	330	8.7 wt%	6 L g^{-1} h^{-1}	150	100%	93%	80	[103]
	NPC700	1143	0.9 at%	0.6 h^{-1}	190	95%	85%	45	[65]
	NrCC-700	2267	3.34 at%	60 L g^{-1} h^{-1}	180	100%	100%	100	[105]
	M/B-1-PZ-700	1269	14.64 wt%	60 L g^{-1} h^{-1}	170	100%	94%	36	[104]
	NC-4-800	352	10.2 at%	60 L g^{-1} h^{-1}	180	100%	90%	160	[107]
	PAM-0.3-700	1727	2.9 at%	40 L g^{-1} h^{-1}	210	96.6 %	82.8 %	80	[106]
	NPC-8	1116	8.0 at%	15 L g^{-1} h^{-1}	190	98%	80%	100	[66]
	H-NC800	1585	/	60 L g^{-1} h^{-1}	190	96.4%	95.0%	80	[108]
	N-S-C-2	356	16.97 at%	40 L g^{-1} h^{-1}	210	94.3%	84.5%	100	[69]
	N-C/CNT-2%P	275	4.8 at%	0.6 h^{-1}	190	85%	93%	100	[68]
	Mn-NDC	392	37.41 wt%	24 L g^{-1} h^{-1}	200	90%	90%	110	[81]
	P-NDC	377	9.02 at%	12 L g^{-1} h^{-1}	260	99.6%	96.1%	60	[70]

2.3. Catalytic Mechanisms of Carbon-Nitrogen Catalysts

2.3.1. $g\text{-}C_3N_4$ Catalysts

The reaction mechanism of H_2S selective oxidation is intrinsically linked to the electronic structure and surface properties of the catalyst. For unmodified $g\text{-}C_3N_4$, its abundance of amino groups facilitates H_2S adsorption as evidenced by in situ Diffuse Reflectance Infrared Fourier Transform Spectroscopy (Figure 14a,b), while the inherent π−conjugated electronic structure leads to a lack of active sites for O_2 adsorption and activation [60,82]. This configuration suggests that the reaction likely follows an Eley−Rideal (E−R) mechanism. In this pathway, H_2S molecules are first activated on the active sites (denoted as X, Equation (4)), subsequently reacting with gaseous O_2 to form elemental sulfur and H_2O, thereby regenerating the active sites and sustaining the catalytic cycle (Equation (5)).

$$2H_2S(g) + 2X \rightarrow 2X{-}H_2S \quad (4)$$

$$2X{-}H_2S + O_2(g) \rightarrow 2X + 2S(g) + 2H_2O(g) \quad (5)$$

Modulation of the π−conjugated system in $g\text{-}C_3N_4$, through strategies such as C doping or the anchoring of metal single atoms, markedly enhances its capacity for O_2 adsorption and activation. For instance, DFT calculations revealed that the adsorption energies of both O_2 and H_2S became more negative on C-doped $g\text{-}C_3N_4$ (E_{ads}−H_2S = −0.51 eV and E_{ads}−O_2 = −0.56 eV) compared to the pristine catalyst (E_{ads}−H_2S = −0.36 eV and E_{ads}−O_2 = −0.05 eV) (Figure 14c). This is further confirmed by TPD experiments (Figure 14d,e) [85]. A similar enhancement in co-adsorption is observed for $g\text{-}C_3N_4$ catalysts

incorporating Fe, Co, or Li single atoms [74,75,88]. Combining with kinetics insights, these findings indicate that the modified catalysts adhere to a Langmuir–Hinshelwood (L–H) mechanism. In this scenario, both O_2 and H_2S molecules are activated on the active sites (Equations (6) and (7)), followed by a surface reaction to yield elemental sulfur and H_2O, completing the catalytic cycle (Equation (8)).

$$2H_2S(g) + 2X \rightarrow 2X–H_2S \quad (6)$$

$$O_2(g) + X \rightarrow X–O_2 \quad (7)$$

$$2X–H_2S + X–O_2 \rightarrow 3X + 2S(g) + 2H_2O(g) \quad (8)$$

Interestingly, diverging from the L–H mechanism proposed by Lei et al., Tong et al. reported, based on DFT calculations, a *quasi* Mars–van Krevelen (MvK) mechanism for g-C_3N_4-supported Fe–N_4 sites. This mechanism involves the reversible extraction and replenishment of protons from the catalyst framework (Figure 14f) [79].

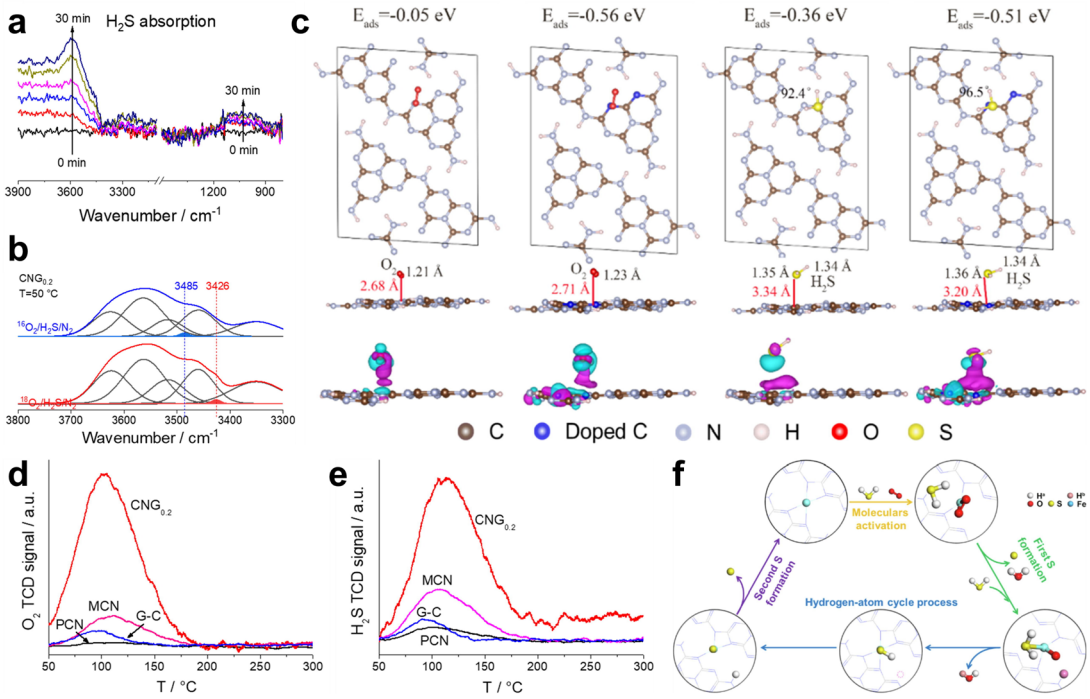

Figure 14. (**a**) In situ DRIFT spectra of the adsorption of H_2S (5% H_2S/95% N_2) on $CNG_{0.2}$ at 200 °C. (**b**) SSITKA-DRIFTS spectra recorded after 20 min of $^{16}O_2/H_2S/N_2$ reaction and after 20 min of the isotopic switch to $^{18}O_2/H_2S/N_2$ over the $CNG_{0.2}$ catalyst at 50 °C, and the deconvolution and curve fitting in the 3800–3300 cm^{-1} range. (**c**) Optimized structures and charge density difference of O_2 and H_2S adsorption on PCN and $CNG_{0.2}$. The violet and blue regions represent electron depletion and accumulation, respectively. The isovalue is 0.00035|e|/Å^3. (**d**) O_2– and (**e**) H_2S-TPD spectra of PCN, $CNG_{0.2}$, G-C, and MCN. Reproduced with permission. Copyright 2022, Elsevier [85]. (**f**) Illustration of quasi-MvK of H_2S selective oxidation on FeN_4-CN. H^a and H^b represent the protons on H_2S and the FeN_4-CN, respectively. Reproduced with permission. Copyright 2022, Elsevier [79].

2.3.2. NDC Catalysts

Analogous to modified g-C_3N_4, NDC catalysts with anchored Mn single atoms also follow an L–H mechanism, with both reactants activated at the Mn sites [81]. Even in the absence of metals, the Lewis basicity of pyridinic N in pure NDC catalysts can, in principle, facilitate the adsorption and activation of both O_2 and H_2S. This is particularly effective in the presence of a surface water film. Under such conditions, H_2S from the gas phase can dissolve into the water film and dissociate into HS^- (Equations (9) and (10)), which can be accelerated by the increased local basicity imparted by Lewis basic nitrogen species. Concurrently, O_2 molecules are adsorbed and activated to form reactive oxygen species (Equation (11)). The subsequent reaction between HS^- and these oxygen species produces elemental sulfur and H_2O, regenerating the active sites and closing the catalytic cycle (Equation (12), Figure 15a) [44,68,69,101].

$$H_2S(g) \rightarrow HS^-(l) + H^+(l) \quad (9)$$

$$HS^-(l) + X \rightarrow X–HS^-(l) \quad (10)$$

$$O_2(g) + X \rightarrow X–O_2(l) \quad (11)$$

$$4X–HS^-(l) + X–O_2(l) \rightarrow 5X + 4S(g) + 2H_2O(g) \quad (12)$$

In the absence of a water film, however, the mechanism can shift. Ye et al. reported that NDC catalysts under dry conditions followed the E–R mechanism

distinct from that of unmodified g-C_3N_4 via TPD experiments, in which the desorption temperature of O_2 molecules was higher than that of H_2S molecules (Figure 15b) [81]. In this case, O_2 molecules are first activated on the active sites (Equation (13)), subsequently reacting with gaseous H_2S to form elemental sulfur and H_2O, achieving the regeneration of active sites and cycle of H_2S-CSO process (Equation (14)) [81].

$$O_2(g) + X \rightarrow 2X{-}O_2 \quad (13)$$

$$X{-}O_2 + 2H_2S(g) \rightarrow X + 2S(g) + 2H_2O(g) \quad (14)$$

Although the MvK mechanism is more characteristic of metal oxides, Liu et al. provided evidence for its operation in NDC catalysts. Specifically, TPD results indicated a lack of O_2 adsorption, thereby ruling out both L–H and E–R pathways. Subsequent TPD-MS experiments revealed reproducible H_2O evolution during cyclic exposure to H_2S and O_2. This suggests that H_2S initially reacts with surface reactive oxygen groups, which are subsequently replenished by O_2 interacting with carbon defects (Figure 15c–e). In essence, the oxygen functional groups on the NDC surface function analogously to lattice oxygen in metal oxide catalysts [99].

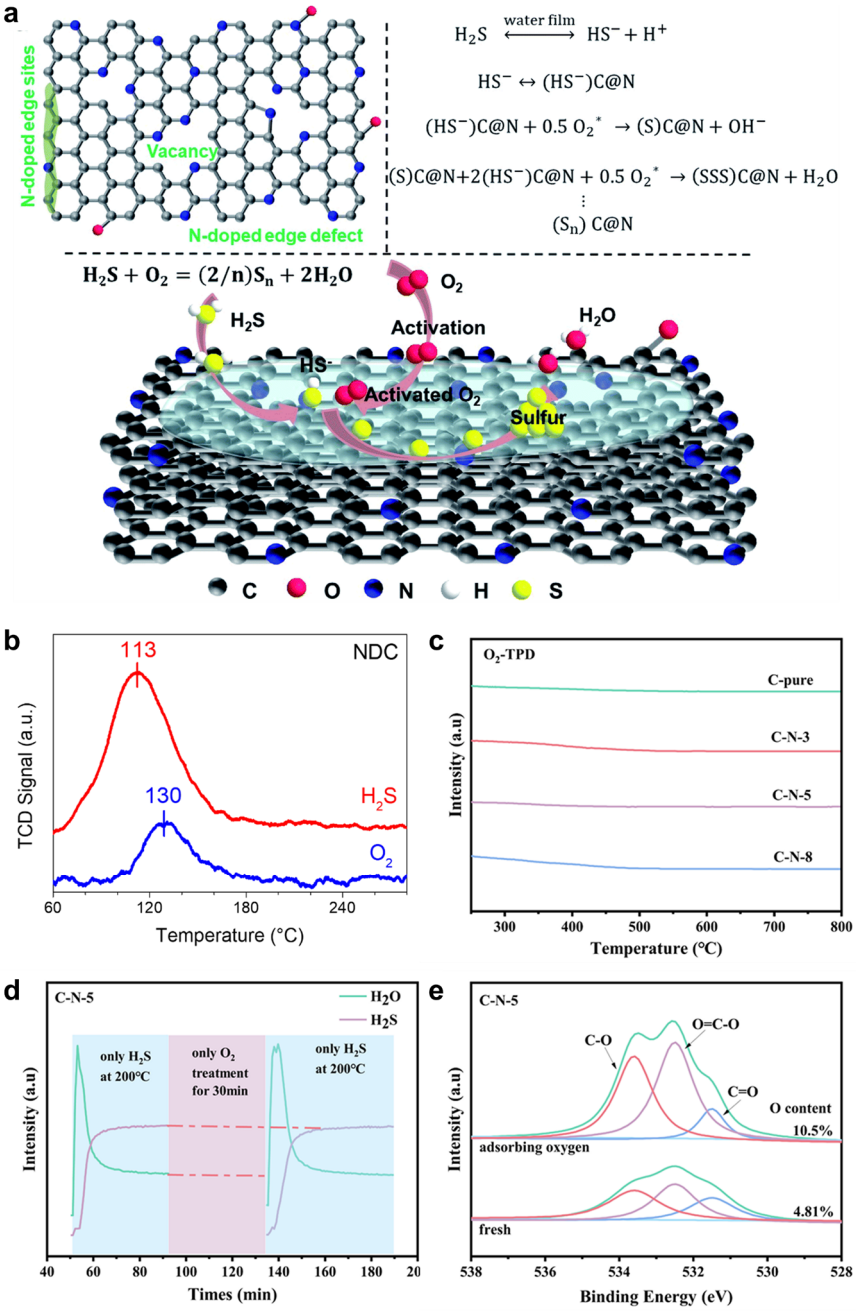

Figure 15. (**a**) Schematic illustration of H_2S-CSO mechanism on the defect enriched N-doped carbon nanoflake model in the presence of water steam. Reproduced with permission. Copyright 2020, Wiley-VCH [44]. (**b**) TPD spectra of H_2S and O_2 towards NDC catalyst. Reproduced with permission. Copyright 2025, Wiley-VCH [81]. (**c**) O_2-TPD of C-N-x catalysts. (**d**) Reactive oxygen species validation experiment of C-N-5. (**e**) O 1s XPS spectra before and after adsorption of oxygen of C-N-5 catalyst. Reproduced with permission. Copyright 2025, Elsevier [99].

3. Conclusions and Future Perspectives

Growing environmental and safety concerns regarding H_2S have led to increasingly stringent emission standards. The H_2S-CSO process stands as a promising technology to meet these standards, with its efficacy hinging on advanced catalyst design. Carbon-nitrogen catalysts, encompassing g-C_3N_4 and NDC, have demonstrated exceptional potential due to their versatile synthesis routes, diverse nitrogen active sites, and highly tunable electronic structures. The use of inexpensive precursors in their synthesis underscores a clear pathway toward scalable and practical applications. To enhance catalytic performance, a multitude of modification strategies have been successfully employed. These include elemental doping (with both metal-free heteroatoms and metal single atoms), defect engineering, and optimization of pore structure, electronic configuration, and support interactions. These strategies collectively aim to enhance the adsorption of reactants (H_2S and O_2) and the desorption of sulfur products. Notably, specific approaches have been tailored to maintain superior performance under industrially relevant conditions, including high O_2 concentrations or elevated reaction temperatures. The establishment of structure-activity relationships and the elucidation of reaction mechanisms have been greatly facilitated by the integration of kinetic studies, in situ characterization techniques, and DFT calculations.

Despite significant progress, several challenges remain: (i) The formation mechanisms of active sites in carbon-nitrogen catalysts are not fully elucidated, impeding the precise and uniform control of key sites, such as pyridinic N in NDC catalysts; (ii) The field employs a wide variety of catalyst morphologies (e.g., bulk, nanotubes, nanofibers) derived from disparate precursors. The lack of comparative studies using consistent material categories hinders a clear understanding of the specific role of morphology. Future research should focus on the rational design of well-defined catalytic centers through advanced synthetic methodologies and operando characterization. Concurrently, establishing robust morphology-activity relationships will provide crucial guidance for utilizing other inexpensive and eco-friendly precursors, forming a solid foundation for industrial application. The integration of high-throughput computational modeling and machine learning is poised to further accelerate the discovery of next-generation carbon-nitrogen catalysts with tailored active sites and optimized reaction pathways, ultimately enabling efficient and sustainable H_2S conversion and sulfur recovery.

Author Contributions

H.Y.: Data curation, Writing—original draft preparation; F.Z., S.L. and Z.W.: Investigation, Writing—editing & proofreading, Supervision; D.W. and C.Y.: Supervision, Writing— review, editing. All authors have read and agreed to the published version of the manuscript.

Funding

This work was financially supported by the National Key Technologies R & D Program of China (2018YFA0209300), the National Natural Science Foundation of China (22272027, U21A20326, and U24A20567), Natural Science Foundation of Fujian Province (2022J01534), 111 Talent Project (D16008), and Taiyuan University of Science and Technology Scientific Research Initial Funding (20252113). C. Y. also thanks the support from the Eyas Program of Fujian Province.

Institutional Review Board Statement

Not applicable.

Informed Consent Statement

Not applicable.

Data Availability Statement

Not applicable.

Conflicts of Interest

The authors declare no conflict of interest.

Use of AI and AI-Assisted Technologies

No AI tools were utilized for this paper.

References

1. Wang, Y.; Chen, X.; Shi, H.; et al. Catalytic reforming of methane with H_2S via dynamically stabilized sulfur on transition metal oxides and sulfides. *Nat. Catal.* **2023**, *6*, 204–214.
2. Zhao, F.; Wang, C.; Xiong, R.; et al. Crystal Engineering of $BiVO_4$ for Photochemical Sensing of H_2S Gas at Ultra-low Concentration. *Angew. Chem. Int. Ed.* **2023**, *62*, e202314891.
3. Zhang, C.; Li, A.-Z.; Yuan, B.-J.; et al. Electrochemical valorization of H_2S in natural gas to sulfate under mild conditions. *Nat. Commun.* **2025**, *16*, 7175.
4. Guidotti, T.L. Hydrogen sulfide: Advances in understanding human toxicity. *Int. J. Toxicol.* **2010**, *29*, 569–581.
5. Behl, M.; Yeom, J.; Lineberry, Q.; et al. A regenerable oxide-based H_2S adsorbent with nanofibrous morphology. *Nat. Nanotechnol.* **2012**, *7*, 810–815.
6. Belmabkhout, Y.; Bhatt, P.M.; Adil, K.; et al. Natural gas upgrading using a fluorinated MOF with tuned H_2S and CO_2 adsorption selectivity. *Nat. Energy* **2018**, *3*, 1059–1066.
7. Duan, C.; Kee, R.J.; Zhu, H.; et al. Highly durable, coking and sulfur tolerant, fuel-flexible protonic ceramic fuel cells. *Nature* **2018**, *557*, 217–222.
8. Islamoglu, T.; Chen, Z.; Wasson, M.C.; et al. Metal–Organic Frameworks against Toxic Chemicals. *Chem. Rev.* **2020**, *120*, 8130–8160.

9. Yang, H.; Zeng, L.; Wang, J.; et al. Optimizing the electronic configuration of h-BN for boosting the photocatalytic transformation of acid gases under visible light. *Env. Sci. Adv.* **2024**, *3*, 97–108.
10. Chiappe, C.; Pomelli, C.S. Hydrogen Sulfide and Ionic Liquids: Absorption, Separation, and Oxidation. *Top. Curr. Chem.* **2017**, *375*, 52.
11. Shah, M.S.; Tsapatsis, M.; Siepmann, J.I. Hydrogen Sulfide Capture: From Absorption in Polar Liquids to Oxide, Zeolite, and Metal-Organic Framework Adsorbents and Membranes. *Chem. Rev.* **2017**, *117*, 9755–9803.
12. Yang, H.; Dai, Y.; Zeng, L.; et al. H_2S adsorbed by bismuth oxychloride under room temperature. *Surf. Interfaces* **2024**, *44*, 103663.
13. PiÉPlu, A.; Saur, O.; Lavalley, J.-C.; et al. Claus Catalysis and H_2S Selective Oxidation. *Catal. Rev.* **1998**, *40*, 409–450.
14. Rodriguez, J.A.; Jirsak, T.; Pérez, M.; et al. Studies on the Behavior of Mixed-Metal Oxides and Desulfurization: Reaction of H_2S and SO_2 with Cr_2O_3(0001), MgO(100), and $Cr_xMg_{1-x}O$(100). *J. Am. Chem. Soc.* **2000**, *122*, 12362–12370.
15. Davydov, A.A.; Marshneva, V.I.; Shepotko, M.L. Metal oxides in hydrogen sulfide oxidation by oxygen and sulfur dioxide. *Appl. Catal. A* **2003**, *244*, 93–100.
16. Pandey, R.A.; Biswas, R.; Chakrabarti, T.; et al. Flue Gas Desulfurization: Physicochemical and Biotechnological Approaches. *Crit. Rev. Env. Sci. Tec.* **2005**, *35*, 571–622.
17. Zhang, X.; Tang, Y.; Qu, S.; et al. H_2S-Selective Catalytic Oxidation: Catalysts and Processes. *ACS Catal.* **2015**, *5*, 1053–1067.
18. Steijns, M.; Derks, F.; Verloop, A.; et al. The mechanism of the catalytic oxidation of hydrogen sulfide: II. Kinetics and mechanism of hydrogen sulfide oxidation catalyzed by sulfur. *J. Catal.* **1976**, *42*, 87–95.
19. Zhang, X.; Dou, G.; Wang, Z.; et al. Selective catalytic oxidation of H_2S over iron oxide supported on alumina-intercalated Laponite clay catalysts. *J. Hazard. Mater.* **2013**, *260*, 104–111.
20. Zheng, X.; Li, Y.; Zheng, Y.; et al. Highly Efficient Porous $Fe_xCe_{1-x}O_{2-\delta}$ with Three-Dimensional Hierarchical Nanoflower Morphology for H_2S-Selective Oxidation. *ACS Catal.* **2020**, *10*, 3968–3983.
21. Lei, C.; Zhou, W.; Shen, L.; et al. Enhanced Selective H_2S Oxidation Performance on Mo_2C-Modified g-C_3N_4. *ACS Sustainable Chem. Eng.* **2019**, *7*, 16257–16263.
22. Mohamadalizadeh, A.; Towfighi, J.; Rashidi, A.; et al. Nanoclays as nano adsorbent for oxidation of H_2S into elemental sulfur. *Korean J. Chem. Eng.* **2011**, *28*, 1221–1226.
23. Lee, J.D.; Jun, J.H.; Park, N.-K.; et al. A study on selective oxidation of hydrogen sulfide over zeolite-NaX and-KX catalysts. *Korean J. Chem. Eng.* **2005**, *22*, 36–41.
24. Zheng, X.; Shen, L.; Lin, F.; et al. Bimetallic Metal–Organic Frameworks MIL-53(xAl–yFe) as Efficient Catalysts for H_2S Selective Oxidation. *Inorg. Chem.* **2022**, *61*, 3774–3784.
25. Peng, W.-L.; Kan, X.; Chen, W.; et al. Efficiently Selective Oxidation of H_2S to Elemental Sulfur over Covalent Triazine Framework Catalysts. *ACS Appl. Mater. Interfaces* **2021**, *13*, 34124–34133.
26. Zhang, X.; Wang, Z.; Tang, Y.; et al. Catalytic behaviors of combined oxides derived from Mg/Al_xFe_{1-x}–Cl layered double hydroxides for H_2S selective oxidation. *Catal. Sci. Technol.* **2015**, *5*, 4991–4999.
27. Bartholomew, C.H. Mechanisms of catalyst deactivation. *Appl. Catal. A* **2001**, *212*, 17–60.
28. Yang, L.; Wang, S.; Blinn, K.; et al. Enhanced Sulfur and Coking Tolerance of a Mixed Ion Conductor for SOFCs: $BaZr_{0.1}Ce_{0.7}Y_{0.2-x}Yb_xO_{3-\delta}$. *Science* **2009**, *326*, 126–129.
29. Argyle, M.; Bartholomew, C. Heterogeneous Catalyst Deactivation and Regeneration: A Review. *Catalysts* **2015**, *5*, 145–269.
30. Boldrin, P.; Ruiz-Trejo, E.; Mermelstein, J.; et al. Strategies for Carbon and Sulfur Tolerant Solid Oxide Fuel Cell Materials, Incorporating Lessons from Heterogeneous Catalysis. *Chem. Rev.* **2016**, *116*, 13633–13684.
31. Lin, T.; Chen, I.W.; Liu, F.; et al. Nitrogen-doped mesoporous carbon of extraordinary capacitance for electrochemical energy storage. *Science* **2015**, *350*, 1508–1513.
32. Titirici, M.M.; White, R.J.; Brun, N.; et al. Sustainable carbon materials. *Chem. Soc. Rev.* **2015**, *44*, 250–290.
33. Bai, X.; Hu, P.; Li, A.; et al. Nitrogen-doped amorphous monolayer carbon. *Nature* **2024**, *634*, 80–84.
34. Adib, F.; Bagreev, A.; Bandosz, T.J. Adsorption/Oxidation of Hydrogen Sulfide on Nitrogen-Containing Activated Carbons. *Langmuir* **2000**, *16*, 1980–1986.
35. Bagreev, A.; Angel Menendez, J.; Dukhno, I.; et al. Bituminous coal-based activated carbons modified with nitrogen as adsorbents of hydrogen sulfide. *Carbon* **2004**, *42*, 469–476.
36. Bashkova, S.; Baker, F.S.; Wu, X.; et al. Activated carbon catalyst for selective oxidation of hydrogen sulphide: On the influence of pore structure, surface characteristics, and catalytically-active nitrogen. *Carbon* **2007**, *45*, 1354–1363.
37. Brazhnyk, D.V.; Zaitsev, Y.P.; Bacherikova, I.V.; et al. Oxidation of H_2S on activated carbon KAU and influence of the surface state. *Appl. Catal. B* **2007**, *70*, 557–566.
38. Duong-Viet, C.; Liu, Y.; Ba, H.; et al. Carbon nanotubes containing oxygenated decorating defects as metal-free catalyst for selective oxidation of H_2S. *Appl. Catal. B* **2016**, *191*, 29–41.
39. Bian, C.; Gao, Q.; Zhang, J.; et al. Impact of pyrone group on H_2S catalytic oxidization. *Sci. Total Environ.* **2019**, *695*, 133875.
40. Klein, J.; Henning, K.-D. Catalytic oxidation of hydrogen sulphide on activated carbons. *Fuel* **1984**, *63*, 1064–1067.
41. Feng, W.; Kwon, S.; Borguet, E.; et al. Adsorption of Hydrogen Sulfide onto Activated Carbon Fibers: Effect of Pore Structure and Surface Chemistry. *Environ. Sci. Technol.* **2005**, *39*, 9744–9749.
42. Chen, Q.; Wang, Z.; Long, D.; et al. Role of Pore Structure of Activated Carbon Fibers in the Catalytic Oxidation of H_2S. *Ind. Eng. Chem. Res.* **2010**, *49*, 3152–3159.
43. Sun, F.; Liu, J.; Chen, H.; et al. Nitrogen-Rich Mesoporous Carbons: Highly Efficient, Regenerable Metal-Free Catalysts for Low-Temperature Oxidation of H_2S. *ACS Catal.* **2013**, *3*, 862–870.
44. Li, S.; Gu, Q.; Cao, N.; et al. Defect enriched N-doped carbon

nanoflakes as robust carbocatalysts for H_2S selective oxidation. *J. Mater. Chem. A* **2020**, *8*, 8892–8902.
45. Jones, D.I.; Stewart, A.D. Properties of hydrogenated amorphous carbon films and the effects of doping. *Philos. Mag. B* **1982**, *46*, 423–434.
46. Kaufman, J.H.; Metin, S.; Saperstein, D.D. Symmetry breaking in nitrogen-doped amorphous carbon: Infrared observation of the Raman-active G and D bands. *Phys. Rev. B* **1989**, *39*, 13053–13060.
47. Panchakarla, L.S.; Govindaraj, A.; Rao, C.N.R. Nitrogen- and Boron-Doped Double-Walled Carbon Nanotubes. *ACS Nano* **2007**, *1*, 494–500.
48. Bagreev, A.; Bandosz, T.J. Study of Hydrogen Sulfide Adsorption on Activated Carbons Using Inverse Gas Chromatography at Infinite Dilution. *J. Phys. Chem. B* **2000**, *104*, 8841–8847.
49. Wu, X.; Schwartz, V.; Overbury, S.H.; et al. Desulfurization of Gaseous Fuels Using Activated Carbons as Catalysts for the Selective Oxidation of Hydrogen Sulfide. *Energy Fuels* **2005**, *19*, 1774–1782.
50. Zheng, X.-X.; Shen, L.-J.; Chen, X.-P.; et al. Amino-Modified Fe-Terephthalate Metal–Organic Framework as an Efficient Catalyst for the Selective Oxidation of H_2S. *Inorg. Chem.* **2018**, *57*, 10081–10089.
51. Yang, C.-M.; Kaneko, K. Nitrogen-Doped Activated Carbon Fiber as an Applicant for NO Adsorbent. *J. Colloid Interface Sci.* **2002**, *255*, 236–240.
52. Gong, K.; Du, F.; Xia, Z.; et al. Nitrogen-Doped Carbon Nanotube Arrays with High Electrocatalytic Activity for Oxygen Reduction. *Science* **2009**, *323*, 760–764.
53. Chizari, K.; Deneuve, A.; Ersen, O.; et al. Nitrogen-Doped Carbon Nanotubes as a Highly Active Metal-Free Catalyst for Selective Oxidation. *ChemSusChem* **2012**, *5*, 102–108.
54. Fujisaki, T.; Ikeda, K.; Staykov, A.T.; et al. Density functional theory analysis for H_2S adsorption on pyridinic N- and oxidized N-doped graphenes. *RSC Adv.* **2022**, *12*, 19955–19964.
55. Zhang, Z.; Zhang, F.; Song, Z.; et al. Oxygen Reduction Reaction on Pyridinic Nitrogen-Functionalized Carbon: Active Site Quantification and Effects of Lewis Basicity. *ACS Catal.* **2025**, *15*, 296–309.
56. Guo, D.; Shibuya, R.; Akiba, C.; et al. Active sites of nitrogen-doped carbon materials for oxygen reduction reaction clarified using model catalysts. *Science* **2016**, *351*, 361–365.
57. Ghasemy, E.; Motejadded, H.B.; rashidi, A.; et al. N-doped CNT nanocatalyst prepared from camphor and urea for gas phase desulfurization: Experimental and DFT study. *J. Taiwan Inst. Chem. Eng.* **2018**, *85*, 121–131.
58. Wang, X.; Maeda, K.; Thomas, A.; et al. A metal-free polymeric photocatalyst for hydrogen production from water under visible light. *Nat. Mater.* **2009**, *8*, 76–80.
59. Lei, G.; Dai, Z.; Fan, Z.; et al. Porous nanosheets of carbon-conjugated graphitic carbon nitride for the oxidation of H_2S to elemental sulfur. *Carbon* **2019**, *155*, 204–214.
60. Shen, L.; Lei, G.; Fang, Y.; et al. Polymeric carbon nitride nanomesh as an efficient and durable metal-free catalyst for oxidative desulfurization. *Chem. Commun.* **2018**, *54*, 2475–2478.
61. Ong, W.-J.; Tan, L.-L.; Ng, Y.H.; et al. Graphitic Carbon Nitride ($g\text{-}C_3N_4$)-Based Photocatalysts for Artificial Photosynthesis and Environmental Remediation: Are We a Step Closer To Achieving Sustainability? *Chem. Rev.* **2016**, *116*, 7159–7329.
62. Lei, G.; Qi, S.; Li, H.; et al. Carbon-doped boron nitride nanosheets as an efficient metal-free catalyst for the selective oxidation of H_2S. *Phys. Chem. Chem. Phys.* **2023**, *25*, 32317–32322.
63. Mi, J.; Liu, F.; Chen, W.; et al. Design of Efficient, Hierarchical Porous Polymers Endowed with Tunable Structural Base Sites for Direct Catalytic Elimination of COS and H_2S. *ACS Appl. Mater. Interfaces* **2019**, *11*, 29950–29959.
64. Yang, C.; Ye, H.; Byun, J.; et al. N-Rich Carbon Catalysts with Economic Feasibility for the Selective Oxidation of Hydrogen Sulfide to Sulfur. *Environ. Sci. Technol.* **2020**, *54*, 12621–12630.
65. Xu, C.; Chen, J.; Li, S.; et al. N-doped honeycomb-like porous carbon derived from biomass as an efficient carbocatalyst for H_2S selective oxidation. *J. Hazard. Mater.* **2021**, *403*, 123806.
66. Zhang, X.; Xu, C.; Li, S.; et al. N-doped porous carbocatalyst engineering via modulating the crystalline size of ZIF-8 for continuous H_2S selective oxidation. *Appl. Mater. Today* **2021**, *25*, 101228.
67. Liu, X.; Zhangsun, G.; Zheng, Y.; et al. Hierarchical N-Doped Carbons Endowed with Structural Base Sites toward Highly Selective Adsorption and Catalytic Oxidation of H_2S. *Ind. Eng. Chem. Res.* **2021**, *60*, 2101–2111.
68. Xu, C.; Gu, Q.; Li, S.; et al. Heteroatom-Doped Monolithic Carbocatalysts with Improved Sulfur Selectivity and Impurity Tolerance for H_2S Selective Oxidation. *ACS Catal.* **2021**, *11*, 8591–8604.
69. Liu, X.; Zhai, X.; Zhao, Y.; et al. Sulfur modified N-doped carbocatalysts promote the selectivity for H_2S selective oxidation. *Appl. Catal. B* **2025**, *362*, 124717.
70. Ye, H.; Zhou, M.; Zeng, F.; et al. Functional carbon materials with Lewis pairs for efficiently transforming sulfur compounds from waste to chemical. *Appl. Catal. B* **2025**, *374*, 125399.
71. Li, S.; Liu, Y.; Gong, H.; et al. N-Doped 3D Mesoporous Carbon/Carbon Nanotubes Monolithic Catalyst for H_2S Selective Oxidation. *ACS Appl. Nano Mater.* **2019**, *2*, 3780–3792.
72. Wang, A.; Li, J.; Zhang, T. Heterogeneous Single-Atom Catalysis. *Nat. Rev. Chem.* **2018**, *2*, 65–81.
73. Lei, G.; Zhao, W.; Shen, L.; et al. Isolated iron sites embedded in graphitic carbon nitride ($g\text{-}C_3N_4$) for efficient oxidative desulfurization. *Appl. Catal. B* **2020**, *267*, 118663.
74. Lei, G.; Tong, Y.; Shen, L.; et al. Highly Active and Sulfur-Resistant $Fe\text{–}N_4$ Sites in Porous Carbon Nitride for the Oxidation of H_2S into Elemental Sulfur. *Small* **2020**, *16*, 2003904.
75. Lei, G.; Tong, Y.; Shen, L.; et al. Highly Poison-Resistant Single-Atom $Co\text{–}N_4$ Active Sites with Superior Operational Stability over 460 h for H_2S Catalytic Oxidation. *Small* **2021**,

17, 2104939.
76. Liu, Y.; Song, C.; Wang, Y.; et al. Rational designed Co@N-doped carbon catalyst for high-efficient H_2S selective oxidation by regulating electronic structures. *Chem. Eng. J.* **2020**, *401*, 126038.
77. Li, Y.; Huang, B.; Li, H.; et al. The effect of coordination states of cobalt on Co-N_x co-doped graphene for selective oxidation of H_2S: A DFT study. *Diam. Relat. Mat.* **2023**, *140*, 110477.
78. Li, Y.; Yang, Y.; Li, K.; et al. Theoretical analysis of selective catalytic oxidation of H_2S on Fe-N_3 co-doped graphene. *Mol. Catal.* **2022**, *524*, 112318.
79. Tong, Y.; Wei, C.; Wang, J.; et al. Microscopic functionality of FeN_4 sites in polymeric carbon nitride for efficient H_2S oxidation. *Appl. Surf. Sci.* **2022**, *600*, 154011.
80. Ghasemy, E.; Emrooz, H.B.M.; Rashidi, A.; et al. Highly uniform molybdenum oxide loaded N-CNT as a remarkably active and selective nanocatalyst for H_2S selective oxidation. *Sci. Total Environ.* **2020**, *711*, 134819.
81. Ye, H.; Xing, W.; Zhao, F.; et al. Sabatier Optimal of Mn-N_4 Single Atom Catalysts for Selective Oxidative Desulfurization. *Angew. Chem. Int. Ed.* **2025**, *64*, e202419630.
82. Lei, G.; Cao, Y.; Zhao, W.; et al. Exfoliation of Graphitic Carbon Nitride for Enhanced Oxidative Desulfurization: A Facile and General Strategy. *ACS Sustainable Chem. Eng.* **2019**, *7*, 4941–4950.
83. Zhong, K.; Zhu, X.; Yang, J.; et al. Ultrathin structure of oxygen doped carbon nitride for efficient CO_2 photocatalytic reduction. *Nanotechnology* **2022**, *33*, 115404.
84. Kamali, F.; Eskandari, M.M.; Rashidi, A.; et al. Nanorod carbon nitride as a carbo catalyst for selective oxidation of hydrogen sulfide to sulfur. *J. Hazard. Mater.* **2019**, *364*, 218–226.
85. Lyu, S.; Wu, W.; Xiong, R.; et al. Carbon-Rich carbon nitride nanocatalysts for H_2S selective oxidation. *J. Catal.* **2022**, *413*, 992–1004.
86. Shen, L.; Lei, G.; Zheng, Y.; et al. Electronic Regulation of Bromophenyl Grafted Metal-Free Carbon Nitride Catalysts for Enhanced Utilization of H_2S. *ChemCatChem* **2021**, *13*, 2386–2392.
87. Gao, C.; Low, J.; Long, R.; et al. Heterogeneous Single-Atom Photocatalysts: Fundamentals and Applications. *Chem. Rev.* **2020**, *120*, 12175–12216.
88. Lyu, S.; Wang, J.; Zhou, Y.; et al. Structural Lithium Incorporated with the Crystalline Poly(Triazine Imide) Frameworks for Selective Catalytic Oxidative Desulfurization. *Adv. Funct. Mater.* **2024**, *34*, 2310286.
89. Shinkarev, V.V.; Glushenkov, A.M.; Kuvshinov, D.G.; et al. Nanofibrous carbon with herringbone structure as an effective catalyst of the H_2S selective oxidation. *Carbon* **2010**, *48*, 2004–2012.
90. Truong-Huu, T.; Duong-Viet, C.; Duong-The, H.; et al. Radiofrequency-driven selective oxidation of H_2S on hierarchical metal-free catalyst containing defects. *Appl. Catal. A* **2021**, *620*, 118171.
91. Housseinou, B.; Cuong, D.-V.; Liu, Y.; et al. Nitrogen-doped carbon nanotube spheres as metal-free catalysts for the partial oxidation of H_2S. *C.R. Chim.* **2016**, *19*, 1303–1309.
92. Duong-Viet, C.; Ba, H.; Liu, Y.; et al. Nitrogen-doped carbon nanotubes on silicon carbide as a metal-free catalyst. *Chin. J. Catal.* **2014**, *35*, 906–913.
93. Duong-Viet, C.; Nhut, J.-M.; Truong-Huu, T.; et al. A nitrogen-doped carbon-coated silicon carbide as a robust and highly efficient metal-free catalyst for sour gas desulfurization in the presence of aromatics as contaminants. *Catal. Sci. Technol.* **2020**, *10*, 5487–5500.
94. Cuong, D.-V.; Truong-Phuoc, L.; Tran-Thanh, T.; et al. Nitrogen-doped carbon nanotubes decorated silicon carbide as a metal-free catalyst for partial oxidation of H_2S. *Appl. Catal. A* **2014**, *482*, 397–406.
95. Wang, W.; Duong-Viet, C.; Truong-Phuoc, L.; et al. Improving catalytic performance via induction heating: Selective oxidation of H_2S on a nitrogen-doped carbon catalyst as a model reaction. *New J. Chem.* **2023**, *47*, 1105–1116.
96. Duong-Viet, C.; Nhut, J.-M.; Truong-Huu, T.; et al. Tailoring Properties of Metal-Free Catalysts for the Highly Efficient Desulfurization of Sour Gases under Harsh Conditions *Catalysts* [Online], 2021, p. 226.
97. Wang, T.; Liu, X.; Shan, L.; et al. Manipulation of Waste-Activated Carbon Absorbers as Efficient Carbocatalysts for H_2S Selective Oxidation. *Ind. Eng. Chem. Res.* **2024**, *63*, 4380–4389.
98. Liu, Y.; Duong-Viet, C.; Luo, J.; et al. One-Pot Synthesis of a Nitrogen-Doped Carbon Composite by Electrospinning as a Metal-Free Catalyst for Oxidation of H_2S to Sulfur. *ChemCatChem* **2015**, *7*, 2957–2964.
99. Liu, X.; Zhao, M.; Liu, D.; et al. Boosting catalytic oxidation of H_2S over activated carbon optimized by the synergistic effect of rich defects and nitrogen sites. *Surf. Interfaces* **2025**, *68*, 106672.
100. Liu, X.; Shan, L.; Sun, X.; et al. Reusable salt-template strategy for synthesis of porous nitrogen-rich carbon boosts H_2S selective oxidation. *Green Energy Environ.* **2024**, *9*, 1866–1877.
101. Liu, X.; Zhao, Y.; Ma, J.; et al. Defects mediate the active N sites in N-doped carbon catalyst for efficiently catalyzing H_2S to element sulfur. *Appl. Catal. B* **2026**, *380*, 125718.
102. Kan, X.; Chen, X.; Chen, W.; et al. Nitrogen-Decorated, Ordered Mesoporous Carbon Spheres as High-Efficient Catalysts for Selective Capture and Oxidation of H_2S. *ACS Sustainable Chem. Eng.* **2019**, *7*, 7609–7618.
103. Lei, G.; Fan, Z.; Hou, Y.; et al. Facile template-free synthesis of 3D cluster-like nitrogen-doped mesoporous carbon as metal-free catalyst for selective oxidation of H_2S. *J. Environ. Chem. Eng.* **2023**, *11*, 109095.
104. Kim, S.Y.; Phule, A.D.; Yang, J.H.; et al. Improving H_2S remediation efficiency through metal-free biochar modification: Nitrogen introduction and mesopore formation. *J. Anal. Appl. Pyrolysis* **2024**, *183*, 106822.
105. Yang, J.; Cui, S.; Zhao, F.; et al. Waste to Wealth: Discarded Cigarette Butt-Derived Metal-Free N-Rich Carbon Catalysts for the Selective Catalytic Oxidation of Hydrogen Sulfide to Sulfur. *Environ. Sci. Technol.* **2024**, *58*, 20267–20276.

106. Li, S.; Fu, H.; Zhang, X.; et al. Hierarchically porous, N-defect enriched C-nanosheets boost the H_2S selective oxidation to elemental sulfur. *Appl. Catal. B* **2024**, *343*, 123505.
107. Li, H.; Zhao, J.; Pan, S.; et al. Template-free fabrication of nitrogen-doped mesoporous carbon catalysts with high water resistance for selective catalytic oxidation of H_2S. *Appl. Surf. Sci.* **2025**, *693*, 162703.
108. Shan, L.; Liu, X.; Zhao, Y.; et al. Hierarchical Porous N-Doped Carbon Particles Derived from ZIF-8 as Highly Efficient H_2S Selective Oxidation Catalysts. *ACS Appl. Mater. Interfaces* **2024**, *16*, 23314–23324.
109. Chung, W.J.; Griebel, J.J.; Kim, E.T.; et al. The Use of Elemental Sulfur as An Alternative Feedstock for Polymeric Materials. *Nat. Chem.* **2013**, *5*, 518–524.
110. Boyd, D.A. Sulfur and Its Role In Modern Materials Science. *Angew. Chem. Int. Ed.* **2016**, *55*, 15486–15502.